This is the peer-reviewed, final accepted version for American Mineralogist, published by the Mineralogical Society of America.
The published version is subject to change. Cite as Authors (Year) Title. American Mineralogist, in press.
DOI: https://doi.org/10.2138/am-2021-7902. http://www.minsocam.org/

Revision 2 –

Word count: 11058

Interphase misorientation as a tool to study metamorphic reactions and crystallization in geological materials

Luiz F. G. Morales [a,b]

[a] Scientific Center for Optical and Electron Microscopy (ScopeM), ETH Zürich, Otto-Stern-Weg 3, 8093, Zürich.

[b] Geological Institute, Department of Earth Sciences, ETH Zürich, Sonneggstrasse 5, 8092 Zurich

Email: luiz.morales@scopem.ethz.ch

Abstract

Interphase boundaries are planar defects that separate two different minerals, which in general have different compositions and/or crystalline structures; they may play an important role as a pathway for fluids in rocks and affect their physical properties. In order to completely characterize interphase boundaries, one needs to define the misorientation between adjacent grains and the orientation of the grain boundary plane. The analysis performed here is limited to the misorientation characterization and the trace of the interphase boundary. Although the determination of possible orientation relationships between the two adjacent phases is routinely performed by selected area electron diffraction in the transmission electron microscope, this method lacks statistical representativeness. With the advent of techniques like electron backscatter diffraction (EBSD), it is possible to calculate orientation relationships not only in single pairs of crystals of the same phase but in full thin sections and between different minerals. The

interphase misorientation is calculated from two orientations of two adjacent crystals of different phases. A set of single misorientations is then used to calculate the misorientation distribution function (MDF), from where it is possible to identify a maximum, and its crystallographic interpretation. If we then know the misorientation and the unit cell parameters of the individual phases, the crystallographic relationships between the different phases can be described with the pairs of parallel crystallographic planes and the pairs of crystallographic directions. We present examples of the use of interphase misorientation analysis on the transformation of calcite-aragonite, olivine-antigorite, magnetite-hematite, and on the study of orientation relationships between plagioclase-olivine-ilmenite in mid-ocean ridges gabbros (ODP Hole 735).

Keywords

Interphase misorientation; EBSD; orientation relationships; phase transformation

INTRODUCTION

Polycrystalline material such as rocks, metals and ceramics are made of different grains with different crystal orientations. Where those grains meet each other, there is normally an interatomic mismatch between the lattices of the two adjacent crystals, which is called grain or phase boundaries. Grain and phase boundaries are a very important part of the microstructure of rocks because they are high diffusivity paths for both fluid and solid-state diffusion. They play an important role on the rheology of rocks and influence petrophysical properties, such as strength of rocks, resistance to cracking and permeability. As grain and phase boundaries are relatively disordered structures, they can accommodate large amounts of impurities, which may influence, for example, boundary migration

Grain boundaries are interfaces that separate grains of the same phase (e.g., quartz grain boundaries), whereas phase boundaries separate grains of different compositions and/or structure (e.g., quartz-feldspar

or calcite-aragonite phase boundaries). The structure and energy of grain boundaries are defined by the misorientation of the two neighboring grains and the orientation of the boundary plane itself. To fully define a grain boundary, one must define 5 variables related to the grain boundary misorientation angle, misorientation axes and the orientation of the interface itself. Standard classification of grain boundaries distinguishes two end members, named tilt and twist boundaries. In tilt boundaries, the rotation axis to bring the lattices of two neighboring crystals into overlap is parallel to the interface plane, whereas in twist boundaries, the rotation axis is normal to the interface, and pretty much all grain boundaries lie in between these two end-members. Grain boundaries are also classified according to the misorientation angle. Adjacent grain boundaries with less than (roughly) 10° misorientation between neighbor grains (the actual angle can be quite variable depending on the crystallographic system) are said to be low angle grain boundaries, while neighboring grain boundaries with higher degrees of misorientations are classified as high angle grain boundaries. In deformed materials, low angle grain boundaries are commonly associated with array of aligned dislocations along a certain plane (forming in this case a "subgrain"). It is important to note that low angle grain boundaries are very important in biomineralization and have nothing to do with intracrystalline defects.

Phase boundaries on the other hand are classified according to the degree of mismatch between the lattices of the two phases along the interface (e.g., Sutton and Baluffi, 1995; Porter and Easterling, 1992). In coherent (or commensurate) phase boundaries (Fig. 1), the two neighbor crystals match perfectly along the interface, and the interfacial plane has the same atomic configuration in both phases. An important aspect of the coherency definition is that the crystallographic plane comprising the phase boundary does not need to be the same in the different phases, but an orientation relationship between the two grains needs to be satisfied. This can be described by a Burgers orientation relationship that specifies a pair of parallel planes and directions, i.e., $(hkl)_{phase\ A} \parallel (hkl)_{phase\ B}$ and $[uvw]_{phaseA} \parallel [uvw]_{phaseB}$ for the general case of single planes and directions. In order to keep the interface coherent, small differences in the lattice parameters between the two phases can be accommodated by elastic strains on both sides separated by the interface.

Such an effect reduces the interface energy at the expense of increasing the internal energy of both phases adjacent to the interface. As such, elastic straining in order to force a perfect coherency only occurs if the interface is strong, if the mismatch is small and if the grain size is small. Although the structure at the interface is perfect, the interfacial energy at the boundary is quite variable, but depends essentially on the composition of the phases separated by the interface. In semi-coherent (or discommensurate) phase boundaries, the elastic strain described previously becomes too large and the lattice mismatch is accommodated by an array of misfit dislocations that do not create long-range strain fields. The total energy of semi-coherent phase boundaries results from both compositional and structural components. In incoherent (or incommensurate) phase boundaries, the different lattices of the two phases at the interface prevents the good matching at the phase boundary, leading to a more disorder structure, similar to those observed in high-angle grain boundaries. The surface energy of both grain and phase boundaries are function of the misorientation angle, and it is known from the materials science literature that during deformation, grain boundaries in metals tend to rotate to minimize such energy, leading to the development of grain boundaries with specific misorientation angles.

Grain boundaries on common minerals such as quartz, olivine and calcite are relatively well understood in different length scales (e.g., McLaren 1986; Faul and Fitz-Gerald 1999; Fliervoet et al., 1999; Wheeler at al. 2001; Bestmann et al. 2004; Lloyd et al. 2004, Hiraga et al. 2004; Wenk et al. 2011, Menegon et al. 2011; Kilian et al. 2011; Krühl et al. 2013 and others). In olivine, for example, special grain boundaries have even been characterized in terms of grain boundary character distribution (Marquardt et al. 2015) and in terms of grain boundary energies (Duyster and Stöckert, 2001). However, although "real" rocks are mostly composed of two or more phases, our understanding of phase boundaries between different minerals is very scarce and predominantly studied at the nanometric scale, with most observations performed with transmission electron microscopes (TEM - e.g., Boudier et al. 2010; Plümper et al. 2011; Obata and Osawa 2011; Marti et al. 2018). Although this is a very powerful tool to investigate interphase boundaries particularly due to its angular resolution (interphase orientations can be determined up to a

105 precision of 0.1°), it has a very limited statistical representativeness, that is because an individual TEM
106 lamella will show at most a few interfaces. However, the TEM is not the only technique available to study
107 orientation relationships between different phases, and any technique involving local diffraction of an
108 electron beam by the crystalline structure of the phases separated by the interface will allow us to calculate
109 the orientation relationship. Here it is proposed to use orientation maps generated via electron backscatter
110 diffraction (EBSD) in a scanning electron microscope (SEM) to calculate the interphase misorientation
111 angle/axis pairs and determine from them potential orientation relationships. It is important to clarify here
112 that the "orientation relationships" described here have a different meaning than that described in
113 crystallography, where there is partial/total coincidence between the lattices of the two materials separated
114 by an interface. Here I use the term in a more "loose" sense, to described that, in certain cases, two
115 different minerals may show some degree of parallelism along certain interfaces without necessarily
116 sharing the same lattice along the interface. Advantages of this method include (i) the higher statistical
117 representativeness of the data, (ii) the potential to calculate the misorientation angle-axis pair of any pair
118 of mineral phases, (iii) the potential to plot phase boundaries with different misorientation angles in the
119 map, and highlight those which have special misorientation angles/axis pairs and even possible orientation
120 relationships and (iv) to use EBSD results and subsequent calculations and then perform more detailed
121 studies of specific interphase boundaries at the TEM scale, preparing TEM lamellae using target
122 preparation with focused ion beam methods. Here I present 4 examples of interphase misorientations and
123 interphase orientation relationships between olivine-antigorite from a serpentinite, calcite-aragonite from
124 high P-T experiments, magnetite-hematite from an undeformed iron ore, and plagioclase-ilmenite
125 relationships from a mid-ocean ridge gabbro. The results are presented in terms of interphase
126 misorientation angles, axes, and plotted directly in the EBSD maps. In order to facilitate the use of this
127 method, a MATLAB script to be used in the MTEX toolbox from Hielscher and Schaeben (2008) is
128 provided as supplementary material.
129

130 **INTERPHASE BOUNDARY MISORIENTATIONS**

Interphase boundary misorientations calculations are relatively new in Earth and Materials Sciences. For instance, McNamara et al. (2012) explored interphase misorientation relationships in the study of crystallographic preferred orientation (CPO) development of barroisite due to mimetic growth at the expense of glaucophane and omphacite. Later, Morales et al. (2018) used the interphase angle/axis pair on the study of olivine-antigorite transformation relationships, where they reported two new orientation relationships never described in the literature. I will briefly review the concept of intraphase misorientation. A complete overview of this topic is given by Wheeler et al. (2001).

Crystal orientations $\boldsymbol{g}$ as determined via EBSD and consistent with the definitions of MTEX can be described as passive rotations $\boldsymbol{r}$ to bring the coordinates from the crystal reference into coordinates in the sample reference frame. Both reference frames are right-handed, the three axes are orthogonal to each other, and both share a common origin for the sake of simplicity (note however that in some cases, the crystal reference frames might not be orthogonal). The rotation angle is always positive if the rotation is counterclockwise when viewed along the rotation axis towards the origin. Using the definitions of Krakow et al. (2017), if we define the specimen reference frame as $\boldsymbol{s}$ and the crystal reference frame as $\boldsymbol{e}$, the rotation has to satisfy

$$r = \boldsymbol{G}.c \qquad (1)$$

where $r=(x,y,z)$ in specimen coordinates and $c=(e_1,e_2,e_3)$, in crystal coordinates. This equation states that a vector e can be transformed into a vector r by an operation $\boldsymbol{G}$, which is a matrix operation.

The misorientation angle in an EBSD map is the angle necessary to bring two adjacent objects of this map (e.g., two neighbor pixels, or two neighbor grains) into coincidence, whereas the misorientation axis is the axis about which this rotation needs to occur to bring the lattices of the two objects into parallelism. These

This is the peer-reviewed, final accepted version for American Mineralogist, published by the Mineralogical Society of America.
The published version is subject to change. Cite as Authors (Year) Title. American Mineralogist, in press.
DOI: https://doi.org/10.2138/am-2021-7902. http://www.minsocam.org/

misorientations $\boldsymbol{M}$ are also passive rotations, but in this case between two crystals reference frames, where the two crystals normally have two different orientations (g_1 & g_2). The misorientation $\boldsymbol{M}$ between these two crystals transforms the crystal coordinates $\boldsymbol{c_1}$ into crystal coordinates $\boldsymbol{c_2}$, as follows (e.g., Krakow et al., 2017)

$$\boldsymbol{M}=\boldsymbol{g_2}^{-1}.\boldsymbol{g_1} \quad (2)$$

and

$$\boldsymbol{M}\boldsymbol{c_1} = \boldsymbol{g_2}^{-1}\boldsymbol{g_1}c_1 = \boldsymbol{g_2}^{-1}\boldsymbol{r} = c_2 \quad (3)$$

When dealing with one single phase, the lattice parameters for the adjacent objects are the same, and so the misorientation axis can be defined by a number of symmetrically equivalent axis/angle pair combinations that are directly dependent on the symmetry of the studied phase. In the case of two neighbor plagioclase (triclinic) grains, there is only one set of misorientation angle/axis capable to bring the lattices of these two grains into coincidence, while in the case of magnetite or garnet (cubic minerals), there are 24 different possibilities (Mainprice et al. 1993; Lloyd et al. 1997; Wheeler et al. 2001). In the case of olivine (orthorhombic) there will be less than 24 possibilities Due to this large number of possibilities in non-triclinic phases, the current convention is to adopt the rotation pair with the minimum misorientation angle(e.g., Morawiec et al., 1995; Wheeler et al. 2001).

On the other hand, when dealing with the misorientation between two phases that belong to different crystallographic systems, the reference misorientation is not unique. Because of that, and due to the fact, that in most cases we will deal with phases of different symmetries, the asymmetric domain for the misorientation axis plots is not ‘fundamental’. That implies that the shape and form of misorientation angle/axis distribution depends on the choice of reference misorientation. If we consider the example of

183 olivine (orthorhombic) and antigorite (monoclinic), the fundamental region requires the entire hemisphere
184 due to the combination of these two different symmetries. In this case, we must define in relation to which
185 crystal reference frame we will plot the misorientation axes. In the case of phase transformations, it makes
186 sense to use the parent phase reference frame, but if one suspects that a different interphase orientation
187 relationship can be deduced from the interphase misorientation data, one has to examine the
188 misorientation axes plot using also the daughter phase reference frame.
189
190 In most of the studies dealing with misorientations, fundamental zones are based on Rodrigues-Frank
191 parameters (e.g., Morawiec, 1997), but in MTEX this construction is based on quaternion geometry (see
192 Krakow et al., 2017 for details). The definition of a particular fundamental zone depends on the alignment
193 of crystal axes and the order in which the symmetry operators are combined for the misorientation
194 calculations. These fundamental zones are calculated by selecting, in a family of symmetrically related
195 equivalent points, the ones with the smallest angle of rotation. If then multiple points have the same
196 distance from the origin, the choice is made based on the direction of the rotation axis.
197
198 Crystallographic point groups control the symmetry operations related to misorientations. If we have
199 misorientation $\boldsymbol{M}$ relating point groups S_1 and S_2 with crystal coordinate systems c_1 and c_2, and using the
200 equation (3), we can write the following expression
201
202 $$\boldsymbol{M} = s_2 \boldsymbol{M} s_1,\ s_1 \in S_1,\ s_2 \in S_2 \qquad (4)$$
203
204 Here we use the smallest unique rotation angle defined as the disorientation angle and the axis of rotation
205 within the inverse pole figure sector that correspond to the point group common to both symmetries,
206 fulfilling the relation $SC = S1 \cap S2$. The fundamental zones for all possible combinations of proper point
207 group symmetry operations are presented in Krakow et al. (2017), but for the sake of simplicity, all the
208 misorientation axes plots are presented in inverse pole figures resulting from those combinations.

DESCRIPTION OF THE SAMPLES

To test the potential of misorientation analysis on the study of metamorphic reactions and magmatic processes, we have studied four different samples (one synthetic and three natural). Three of these samples are known examples of phase transformations or crystallographically controlled metamorphic reactions: (i) calcite-aragonite; (ii) olivine-antigorite and (iii) magnetite-hematite. In all these cases, the neighboring phases that share a common boundary do not belong to the same crystallographic system. The fourth example is an oxide-rich gabbro coming from the Atlantis Bank (Indian Ocean), where I have tested all the possible pairs of 6 different minerals that compose this rock (plagioclase, diopside, olivine, ilmenite, magnetite and pargasite) and I found that plagioclase-olivine and plagioclase-ilmenite have specific misorientation angle/axis pairs that suggests that both olivine and ilmenite crystallized using specific plagioclase crystal planes as substrate.

Calcite - Aragonite phase transformation produced experimentally

The calcite-aragonite aggregated studied here (sample 010-SC-3-X) belong to the collection of deformation experiments performed by Sebastian Cionoiu during his PhD thesis at ETH Zürich, whose objective was to understand the effect of stress on mineral reactions (see thesis volume for sample preparation details). The calcite-aragonite phase transformation observed in this sample occurred under hydrostatic conditions (i.e., no axial load applied) under 1.6 GPa pressure and temperatures of 600°C for about 12 hours. In the studied sample, aragonite comprises about 25 % of the total aggregate and occurs predominantly wrapped around large calcite crystals, as if forming tails of recrystallized material (Fig. 4a). Calcite is heavily twinned and has some undulose extinction, but no clear subgrains or recrystallized grains, and no noticeable grain growth has been observed. Aragonite grain sizes vary from 3 μm to 12 μm

and there is no clear evidence of crystal plasticity in this phase such as undulose extinction or subgrain walls.

Tremolite-chlorite-antigorite schist from Moses Rock (USA)

The sample of tremolite-chlorite-antigorite schist studied here (MR-1) was collected from the Moses Rock dike and was previously studied by Boudier et al. (2010) and Morales et al. (2013). The Moses rock dike belongs to the Navajo Volcanic Field (NVF) that is exposed in the central part of the Colorado Plateau, in the Four-Corners region, SW of USA. The Moses Rock dike belongs to kimberlitic and lamprophyric breccias that contain a large variety of mantle and lower crustal xenoliths of a variety of compositions (Smith, 1995, 2010). The mantle fragments, associated with the subduction of the Farallon slab, include metaperidotites rich in hydrous phases, jadeite clinopyroxenites and eclogites, spinel websterite and spinel lherzolites and were formed at depths between 50 and 150 km and temperatures ~900 °C according to clinopyroxene thermometry (Hunter and Smith, 1981),

Magnetite – hematite phase transformation

The magnetite-hematite studied here was collected in the Corrego do Feijão mine in the western part of the Quadrilátero Ferrífero, southeastern Brazil. This “iron quadrangle” lies within the Cauê formation of the Itabira group, a metasedimantary sequence of Archean/Paleoproterozoic ages that lies on the southern boundary of the São Francisco craton (Alkmin and Marshak, 1998). This sequence hosts large iron ore deposits in the form of itabirites and polycrystalline hematite with variable contents of magnetite. Deformation intensity and metamorphic conditions increases from east to west (Rosière et al., 2001), and the iron ores present a progressive enrichment of hematite with respect to magnetite towards the east. The studied sample is still relatively rich in magnetite and is composed approximately by 60 % magnetite and 40% hematite, with goethite occurring as alteration material.

261

262 **Plagioclase-olivine and plagioclase-ilmenite in an oxide gabbro from the Atlantis Bank**

263

264 The Atlantis bank is an oceanic core complex that was exhumed by a large-scale detachment fault on the
265 Southwest Indian Ridge (Karson and Lawrance 1997, Kelemen et al. 2007). Deformation in these rocks is
266 localized along hypersolidus and HT shear zones, later overprinted by brittle faults of different scales, as
267 detailed described by Miranda et al. (2010) and Allard et al. (2021). Here we studied oxide-rich gabbros
268 that occur with higher frequency toward the top of the borehole and are interpreted to have intruded the
269 more primitive gabbros at a later stage. Composition of the studied samples varies considerably from
270 sample to sample, between clinopyroxene and plagioclase-rich gabbros, but the content of oxides (mostly
271 magnetite and ilmenite) is between 5-10% volume. The studied sample has well-developed foliation, but
272 lineation is not well marked. In general, plagioclase occurs as equigranular aggregates, whereas
273 clinopyroxene occurs predominantly as porphyroclasts. Olivine occurs as equigranular, idiomorphic grains
274 within the gabbros, but also as "pods" rich in olivine in pressure shadows of clinopyroxenes. Ilmenite and
275 magnetite occur along bands parallel or oblique to the foliation.

276

277 **METHODS**

278

279 The crystallographic preferred orientations of the studied samples were determined by electron backscatter
280 diffraction technique (EBSD) in a scanning electron microscope. All the samples were measured in a FEI
281 Quanta 200F with EDAX Hikari EBSD camera operating at the Scientific Centre for Optical and Electron
282 Microscopy (ScopeM) of ETH Zürich. All the samples were mechanically polished to a 0.25 μm diamond
283 suspension and chemically-mechanically polished with an alkaline solution of colloidal silica (0.025 μm)
284 for 3-10 minutes on a neoprene polishing cloth. All the EBSD maps were acquired using an accelerating
285 voltage of 20 kV, beam current of 8 nA, working distance of 17 mm, and variable stepsizes, from 0.5 to 1
286 μm, depending on the scale of the map. With the exception of the olivine-antigorite sample, all the EBSD

maps used 4 x 4 binning of the patterns. The antigorite was indexed using the structure determination proposed by Capitani and Mellini (2006), using an a-axis of 35 Å, typical of high-temperature antigorite. As antigorite generates poor patterns in the above standard EBSD mapping conditions, a binning of 2 x 2 combined with a pixel Hough binning of 160 and about 120 reflectors were used for the correct indexation. Post-acquisition processing in the EDAX-OIM 8 software included the standardization of the confidence index (CI) using a minimum grain tolerance angle of 10°, and minimum 10 indexed pixels per grain, followed by a CI correlation between neighbor points, where pixels with low CI (<0.1) are reassigned to the orientation and the CI of the neighbor data point with highest CI in the individual grains. All the EBSD maps, calculations and plots were carried out with the MTEX toolbox for MATLAB (Hielscher and Schaeben, 2008). The orientation distribution functions (ODFs) were calculated using the complete datasets with the de La Vallee Poussin kernel with a half-width of 10°, which is equivalent of a bandwidth of 28 in the spherical harmonic coefficients. All the data is plotted in equal-area, upper hemisphere pole figures, with a resolution of 5°. Interphase misorientation pairs between phase A and phase B were calculated for the entire maps using a common misorientation threshold of 10°, and therefore low angle interphase misorientations, if present, are not studied here. Detected grains with less than 10 pixels were also not considered in the calculations.

RESULTS

Calcite – Aragonite

In the studied sample, calcite is the dominant phase (~75% sample) while aragonite is secondary (making up the other ~25% volume - Fig. 2a). Calcite grain size varies between 25 μm -120 μm, some of the large grains are heavily twinned, and most of the large calcite grains have large internal misorientations, up to angles of 10° (Fig. 2b). The aragonite occurs predominantly wrapped around the calcite large grains along discontinuous, anastomosing bands (Fig. 2a, c), except for the small aggregate of coarser grain aragonite

313 that occurs in the bottom of the Fig. 2a. It has grain sizes varying from 4 μm to 12 μm, and from the
314 orientation maps, it seems that the crystallographic preferred orientation of both calcite and aragonite is
315 very weak (Fig. 2a, d). This is confirmed on the pole figures (Fig. 3), where both minerals show a certain
316 degree of CPO that is slightly stronger in calcite (4.3 MUD - multiples of uniform distribution) than
317 aragonite (2.6 MUD). The pole figures are also used here to look for possible similarities between
318 different poles of the studied mineral pairs, which may indicate that the development of a CPO of phase 2
319 is crystallographically controlled by phase 1, but do not fully proof that both phases have any orientation
320 relationship along the interfaces . A careful comparison between the pole figures of both phases shows
321 similarities. For instance, the [100] axes of aragonite are distributed in a broad girdle that is parallel to a
322 similar girdle of poles to (2 $\bar{1}$ $\bar{1}$ 0) of calcite, whereas the distribution of [001] of aragonite is similar to
323 the distribution of (0 1 $\bar{1}$ 8) of calcite. In addition, the strongest concentration of [010] and [110] in
324 aragonite are subparallel to the maximum concentrations of (0001) and (1 0 $\bar{1}$ 4) of calcite, respectively.
325
326 The uniform misorientation angle distribution (i.e., the misorientation distribution expected in the case of
327 a uniform, "random" ODF) shows a progressive increase in frequency to a maximum of 90° (Fig. 4a) and
328 a sudden drop to a maximum misorientation angle ~92° (for the trigonal-orthorhombic relationship). The
329 uniform misorientation axis distribution (Fig. 4b) has a weak maximum parallel to the poles of ($\bar{6}$ 2 4 5)
330 and symmetrically related, which are about 10° from the poles to (1 $\bar{2}$ 1 0), with a maximum of uniform
331 distribution (MUD) around 2.5. The misorientation angle distribution for correlated (neighbor) interphase
332 boundaries tend to follow the distribution expected in the case of a uniform distribution (Fig. 4c). In detail
333 however, the red bars that represent the misorientation angle between neighbor phase boundaries show
334 that the peaks between 25° to 50° occur in higher frequencies than the ones expected in the case of non-
335 neighbor pairs (red line) or uniform distribution (orange line). This suggests that phase boundaries within
336 this angle range show some sort of physical relationship that the uncorrelated distribution does not
337 present, which might indicate a special orientation relationship between calcite and aragonite.
338

For the orientation relationship (11-20)calcite || (100)aragonite and [0001]calcite || [110] aragonite, the misorientation axis is 54.2°, and the misorientation axis is parallel to (2 $\bar{1}$ $\bar{1}$ 0) in the calcite reference frame and to (100) in the aragonite reference frame. If we now plot the misorientation axes for the whole range of misorientation angles for the calcite-aragonite phase boundaries, there is a vast distribution around the primitive circle of the steronet and a weak maximum parallel to the pole of (2 $\bar{1}$ $\bar{1}$ 0), in agreement with a dominant topotactic relationship transformation between calcite and aragonite (Fig. 4d). Note that due to the symmetry, only two out of four symmetrically equivalent pole to planes of aragonite are parallel to two out of three pole to planes in calcite, which are $(1\ \bar{1}\ 0\ 8)_{cal}$ || $(\ \bar{1}\ 1\ \bar{3})_{ar}$ and $(\ \bar{1}\ 0\ 1\ \bar{8})_{cal}$ || $(\ \bar{1}\ \bar{1}\ 3)_{ar}$. The interface trace map in the Figure 4e shows a broad range of distribution of misorientation angles for the interface traces, but about 41% of the phase boundaries between calcite and aragonite have a range of misorientations between 40-70°.

Olivine – Antigorite

The sample MR-1 contains about 60% volume of hydrous phases (chlorite, tremolite and antigorite), and about 40% of the lithospheric mantle olivine framework is still preserved (e.g., Fig. 5a). The sample's microstructure is described in details by Morales et al. (2013). The thin section studied here was cut normal to the antigorite foliation and parallel to the dominant lineation. The phase boundaries between olivine and the hydrous phases in this sample are predominantly straight and sharp, while the contacts between hydrous phases might be blurred and difficult to identify visually.

Olivine and antigorite bulk crystallographic preferred orientation is given in the Figure 6. Due to the relatively coarse grains and the dismembering due to the antigorite, the olivine CPO is relatively complex but not very strong (maxima of 3.9 MUD), with [100] orientated around 20° from the antigorite lineation and [010] and [001] distributed along incomplete girdles, normal and parallel to the XZ plane respectively. Antigorite on the other hand has a strong texture (8.5 MUD for (001) and has a typical (001) fiber-texture,

with the poles of (001) strongly orientated at a small angle to the pole of the foliation and the poles of (100) and (010) distributed along girdles parallel to the reference foliation. Although it is not possible to establish clear orientation relationships between olivine and antigorite primary maxima from these figures, in detail the secondary maxima show some similarities. For instance, the secondary maxima of olivine [010] and [001] close to Z is parallel to the maxima of poles to (010) of antigorite.

The uniform misorientation angle distribution for olivine-antigorite (Fig. 7a) shows a progressive increase up to a maximum peak at 90°, when it drops down substantially, reaching a maximum misorientation angle ~120° for the combination of orthorhombic-monoclinic. The uniform misorientation axis distribution (Fig. 7b) shows a maximum peak on <947>, with a MUD 1.6. The correlated misorientation angle distribution shows some peaks that are much higher than the expected distribution of non-correlated phase boundaries or the misorientation expected in the case of uniform ODF. In particular, the misorientation angles between 70°-100° are considerably higher. If the misorientation angle is now limited to this angular range, the resulting misorientation axis plot show a maximum parallel to the poles (094), which lies about 30° from [010]. This is almost equivalent to the [5 $\bar{9}$ 4] axis described in Morales et al. (2018). The interphase boundary map presented in the Figure 7e shows that about 48% of the interfaces between olivine and antigorite have a range of misorientations between 80-100°, from which 27% have a 10° misorientation range of 90-100°.

Magnetite – hematite

In the studied sample, magnetite comprises ~60% volume and hematite ~40% volume and the whole sample present a massive structure. Hematite nevertheless seems to occur in “patches” on the EBSD map (Fig. 8a). Magnetite shows almost uniform distribution of its main crystal directions [100], [110] and [111], with only [100] showing some degree of orientation subparallel to Z in the sample reference frame (Fig. 9a). Hematite CPO on the other hand is stronger (Fig. 9b) and shows a maximum concentration of

poles to (0001) parallel to Y and a more complex distribution of poles of (1 0 $\bar{1}$ 0) and (1 0 $\bar{1}$ 1). At first it seems that is no clear relationships between the pole figures of magnetite and hematite. However, as magnetite is cubic, a rotation of 90° around x in the pole figure is allowed and would bring this maximum into parallelism with hematite (0001) pole figure.

The uniform misorientation angle distribution of magnetite-hematite shows a peak around 42° (Fig. 10 a), followed by a fast drop to the maximum possible interphase misorientation angle between these two phases at 60°. The uniform misorientation axis distribution (Fig. 10b) shows a maximum peak on <231>, with a MUD 3.5. The interphase misorientation angle distribution for neighbor crystals follows the same trend for the uncorrelated grains, or the distribution expected in the case of uniform distribution (Fig. 10c). Nevertheless, it shows frequencies around 5% higher than the frequency expected in the case of uniform distribution. The correlated interphase misorientation axis (Fig. 10d) show a similar distribution as the uniform one, but only one stronger concentration parallel to [231] with MUD of ~8, with the other symmetrically equivalents ([$\bar{3}$ 2 1], [$\bar{2}$ $\bar{3}$ 1],[3 $\bar{2}$ 1]) showing weaker concentrations. The interphase boundary map (Fig. 10e) shows that 73% of the interphase boundaries have misorientations between 30-50°, and 41% lie in a range of 40-50°.

Plagioclase – Olivine – Ilmenite

In the studied sample of gabbro from the Atlantis bank, plagioclase is the dominant phase, and together with clinopyroxene, are the primary phases to crystallize in this sample. Plagioclase are predominantly subhedral, grain size varies from 100 to 600 μm (Fig. 11a) and a considerable number of grains still preserve magmatic twinning. The smaller plagioclase grains are interpreted as plagioclase subgrain rotation recrystallization (Allard et al., 2021). Plagioclase CPO is relatively weak, as seen in the orientation map with a large variety of colors (Fig. 11c). Olivine on the other hand occurs predominantly as anhedral grains that are much smaller in grain sizes (50-100 μm). In this sample, olivine seems to be (at

least in part) a late phase, as it commonly occurs along interstitial spaces between plagioclase and diopside grain/phase boundaries, and along pressure shadows adjacent to clinopyroxene porphyroclasts. Ilmenite grains are mostly anhedral in shape, grain sizes are between 20-70 μm, and occur predominantly in contact with plagioclase (Fig. 11a).

The pole figures for plagioclase, olivine and ilmenite are plotted in a sample reference frame where the foliation is vertical N-S (so the pole of the foliation is at E in the pole figure), and the lineation also N-S, but horizontal (Fig. 12). All the pole figures show a weak crystallographic preferred orientation. Plagioclase (100) poles are distributed along a broad, asymmetrical vertical girdle cross-cutting Y, while the poles to the (010) are mainly concentrated at an angle of ~15° with the pole of foliation. Olivine [100] axes are predominantly concentrated parallel to Y, [010] and [001] broadly distributed with weak maxima parallel to the pole of the foliation (the former) and parallel to the lineation (the latter). The (0001) pole of ilmenite are preferentially aligned with Y, while the poles of the (1 0 $\bar{1}$ 1) rhombs are at low angle with the pole of the foliation Z and the poles to the (1 0 $\bar{1}$ 0) prisms subparallel to the lineation, but showing secondary, symmetrically related maxima every ~60°. However, in this case, similarities between pole figures are more important than CPO strength. For instance, the distribution of [100] and [010] of olivine shows similarities with the (100) and (010) poles of plagioclase, while the poles of (0001) and (10-10) of ilmenite shows similarities with the (100) poles of plagioclase, and the distribution of (10-11) poles of ilmenite are comparable to the poles of the (010) planes of plagioclase (Fig. 12).

The misorientation angle distribution assuming a uniform distribution show, for the plagioclase-olivine, a peak at misorientation angles ~83° and a sudden drop to a maximum misorientation of ~120° (Fig. 13a). Due to the triclinic-orthorhombic combined symmetry (plagioclase-olivine), the misorientation axes have to be presented in both upper and lower hemisphere, where the maximum misorientation angle expected in the case of a uniform distribution is subparallel to the <253> of olivine, with a MUD of 1.7 (Fig. 13b). In the case of plagioclase-ilmenite, the maximum misorientation angle expected in the uniform case is ~90°,

443 with frequencies dropping progressively to a maximum angle of 180° (Fig. 13c). The maximum
444 misorientation angle in the combination of plagioclase-ilmenite symmetries seems to be distributed all
445 over along the primitive circle of the stereonet, and only statistical calculations allows to pinpoint a
446 maximum parallel to the poles to the $\{3\ 2\ \bar{1}\ 0\}$ planes of ilmenite and subparallel to [100] of plagioclase,
447 with a MUD of 3 (Fig. 13d).
448
449 The distribution of interphase misorientation angles for neighbor (correlated) plagioclase-olivine grains
450 show abnormal frequencies for misorientation angles between 65 and 90° (>2% of the
451 uncorrelated/uniform distribution – Fig. 14a). If we limit the range of misorientation angles to the one
452 above and plot the misorientation axes, the orientation is not very strong (2.5 MUD), but it shows a
453 maximum parallel to the pole to the (100) of plagioclase, 2 other maxima with similar MUD, and a
454 secondary maximum parallel to [010] of plagioclase (parallel to the pole to the (010) plane – Fig. 14b).
455 The misorientation angle distribution for the pair plagioclase-ilmenite shows a number of higher
456 frequency peaks intercalated with lower frequency peaks (Fig. 14c), when compared with the
457 uncorrelated/uniform distributions. Also, the studied sample does not show misorientation peaks larger
458 than 165°. For simplicity, we focus on the misorientation peaks between 85-130°. When limited to this
459 range, most of the misorientation axes are parallel to the [100] of plagioclase, with a MUD of 9. The
460 interphase boundary map (Fig. 15a) shows that about 70% of the boundaries between plagioclase and
461 olivine have a narrow range of misorientations between 60 and 100°, while in the case of plagioclase-
462 ilmenite the range is more variable (Fig. 15b), and about 50% of the interphase boundaries between these
463 two phases have a range of misorientations between 60 and 120°.
464
465 **IMPLICATIONS**
466
467 **Easier assessment of interphase boundary orientation relationships**
468

Differently from grain boundaries separating grains of same composition and structure, interphase boundaries are interfaces that normally separate grains with different structures and / or compositions. Because of this complexity, only individual interfaces are normally studied at the time, in most cases via selected area diffraction (SAD) in a transmission electron microscope (TEM). SAD-TEM provides very detailed information in terms of angular and spatial resolution of orientation relationships between the two phases separated by the interface (atomic scale resolution with angular resolutions <0.1 °) at the expenses of statistical representativeness. Electron-transparent sample preparation for TEM is not trivial and for certain geological materials can be challenging. As an example, to prepare standard in-situ TEM lamellae via focused ion beam techniques, one needs around two hours. However, one has to consider that the area of such a sample is around 150 μm^2, and ~100 nm thick, so in the case of a very fine-grained material, one may observe a few interphase boundaries, but in the case of a more coarse-grained rock, one might be able to see only one interface. In addition, TEM operation and correct indexing of diffraction patters from SAD (particularly for low-symmetry phases) is more complex and time consuming than SEM operation and EBSD mapping and require extensive training to be done effectively. As demonstrated here with EBSD maps, one can see a statistically representative number of interfaces on samples that have different phases and different grain sizes. As we know the orientation of the grains separated by the interface, we can then calculate the misorientation angle/axis between these grain pairs, which can be used to infer possible orientation relationships between the two phases. As an example, we know that $(11\text{-}20)_{cal} \parallel (100)_{ara}$ and $[0001]_{cal} \parallel [011]_{ara}$. If we know now the orientation of the daughter phase (in this case, aragonite), we can compute the orientation of the parent phase following the MTEX script presented in the supplementary material.

The intention here is not to say that EBSD-derived interphase misorientation is a substitute for TEM analysis. If fact, the idea is to use EBSD mapping to precisely locate the orientation and misorientation of specific interphase boundaries and use this data to select the interfaces one wants to study in more detail in the TEM. The interphase misorientation analysis does not give us the degree of coherency between the

phases separated by the interface, nor any atomic resolution along the interface separating two minerals. On the other hand, once you have an EBSD map, you can test possible misorientation relationships between any phase present in the map. That was the case of the gabbro sample whose results are presented in the Figs. 11-15, we have tested all the possible pairs of phases within the map and found that plagioclase-olivine and plagioclase-ilmenite have an orientation relationship that can further be analyzed in the TEM.

Interphase orientation relationships

Phase transformations in geological materials leading to interphase orientation relationships between parent→daughter phases occur predominantly by two major mechanisms: martensitic and nucleation/growth mechanisms. From the four different systems studied in this paper, two belong to the nucleation/growth mechanism (olivine→antigorite and magnetite→hematite), one can be either interpreted as a martensitic or nucleation/growth (calcite→aragonite), and are discussed in a bit more detailed below. In fact, martensitic transformations have been referred in the material sciences literature as a type of nucleation/growth type of transformation that occurs in much shorter time scales (e.g., Olson and Morris-Cohen, 1972; Guimarães and Rios, 2008). Plagioclase→olivine and plagioclase→ilmenite on the other hand do not represent phase transformation of any sort, but because the misorientation angle/axis pair show what looks like special relationships, these results are discussed in terms of orientated growth below.

Nucleation and growth mechanisms are normally associated with diffusion and therefore tend to be thermally activated or enhanced. The growth of one phase into another also depends on the interfacial free energy, the Gibbs free energy of the reaction and the strain free energy (e.g., Mainprice et al., 1990, Porter and Easterling, 1992). Phase transformation from parent phase to daughter phase may occur by only changing the structure from the parent phase (e.g., calcite-aragonite) or by changing both the composition

structure between the two phases (e.g., magnetite-hematite or olivine-antigorite). This process starts with the homogenous (or heterogeneous) nucleation of the daughter phase. The homogeneous nucleation is controlled by the energy to form the nucleus of the daughter phase, and because of that, it requires activation energies much higher than those required for heterogeneous nucleation (e.g., Porter and Easterling, 1992; Sunagawa 1994). Heterogeneous nucleation refers to the nucleation of the daughter phase along the parent phase substrate and requires much less activation energy because the interface between the old and new phases reduces considerably the surface energy value. Heterogeneous nucleation normally occurs along intracrystalline defects (dislocations, grain/interphase boundaries) or due to the presence of inclusions, where the initial nuclei of the daughter phases growth normally by diffusion processes.

Classical examples of this mechanism include the hydration of olivine and formation of antigorite and the transformation of magnetite into hematite. Plümper et al. (2012) showed that the initial exchange of Fe-Mg along (100) dislocation walls in olivine lead to the first steps of topotactic formation of antigorite along this plane in olivine, something also observed in Boudier et al. 2010. As demonstrated in the Fig. 7c, the highest frequency interphase misorientation range is between 80-100°, with a dominant misorientation axis parallel to the (094) poles, which departs 15° from the interphase misorientation axes parallel to the (5-94) poles determined in Morales et al. (2018). Considering that the sample studied here is less deformed and has the olivine grain network much better preserved than the antigorite schist investigated in the aforementioned study, we conclude that the interphase misorientation relationships are compatible with the type 4 phase transformation of $(010)_{ol} \parallel (210)_{atg}$ and $[100]_{ol} \parallel [001]_{atg}$, determined by Morales et al. (2018) using the interphase misorientation angle/axes.

Calcite-aragonite transition and the orientation relationships between the two phases has been extensively studied in the past (e.g., Carlson and Rosenfeld, 1981; McTigue and Wenk, 1985; Gillet et al., 1987) and two main mechanisms for the phase transformation has been proposed. While the experimental results

547 suggest that the heterogeneous nucleation and topotactic growth is the dominant mechanism under a
548 variety of conditions, in agreement with the model from Carlson and Rosenfeld (1981), Gillet and Madon
549 (1982) proposed a martensitic mechanism for the calcite-aragonite transition. In this model, stacking faults
550 dragging by partial dislocation movement is responsible for the phase transformation. In contrast to
551 (normally) slow nucleation and growth mechanisms, martensitic phase transition can be a very fast
552 mechanism, normally producing a metastable phase. Martensitic transformation occurs by the progressive
553 and systematic shearing of the lattice of the parent phase in a way that the distance in which any atom
554 moves is less than one atomic spacing, which implies that the lattice is distorted, but the atoms retain the
555 same neighbors. Because of that, martensitic transformation only leads to change in the structure of the
556 phases, and not in composition, in order to accommodate the shearing described above.
557
558 Gillet et al. (1987) described the dominant phase transition orientation relationship for calcite→aragonite
559 as $(11\bar{2}0)_{cal} \parallel (100)_{ara}$ and $[0001]_{cal} \parallel [011]_{ara}$. McTigue and Wenk (1985) on the other hand described
560 $(11\bar{2}0)_{cal} \parallel (010)_{ara}$, $(10\bar{1}4)_{cal} \parallel (011)_{ara}$ and $[r2{:}f1]_{cal} \parallel [001]_{ara}$. The predominant misorientation angle of
561 54.2° with a dominant axis parallel $(2\bar{1}\bar{1}0)$ of calcite reference frame of the studied sample indicate that
562 in general, the transformation orientation relationship in this case is the one described by Gillet et al.
563 (1987). However, when the misorientation angle is limited to a narrow range between 25° and 50°, the
564 misorientation axis change to parallel to the pole to the $(01\bar{1}8)$ which is the twin plane of e-twins in
565 calcite. Although we don't have access to the orientation of the interface along twin planes, it seems from
566 the EBSD map that the red interphase boundary traces are visually subparallel to the twin planes, for
567 example, of the grains on top-left of the map (Fig. 4e). This observation is in agreement with the Fig. 2a-b,
568 where a number of aragonite grains occur wrapped around a heavily twinned calcite grain, and those
569 grains in contact with that specific calcite grain are the ones that produce the misorientation axis
570 subparallel to $(01\bar{1}8)$.
571

572 Transformation from magnetite to hematite is another example of nucleation and growth mechanism,
573 where hematite growths topotactically on magnetite, following the main orientation relationship $(111)_{mag}$ ||
574 $(001)_{hem}$ and $(-101)_{mag}$ ||$(100)_{hem}$ (Heizmann et al., 1981, Lagoeiro, 1998, Barbosa and Lagoeiro, 2010).
575 These authors described other orientation relationships, and the transformation magnetite-hematite-
576 magnetite is, in their case, reversible and always topotactically controlled. The misorientation angle for the
577 topotactic orientation described above is ~56°, and the misorientation axis is parallel to <793> of
578 magnetite, which is about 4° from the direction <231> expected in the case of a uniform distribution (Fig.
579 10b) As we see in the histogram from Figure 10c, all the misorientation angles above 40° occur more
580 frequently than expected in the case of a uniform distribution, with the highest bin showing
581 misorientations between 45-50°. However, the misorientation axis is very close to the one expected in the
582 case of a random orientation of both magnetite and hematite. As demonstrated in the pole figures (Fig. 9),
583 hematite CPO is stronger than magnetite, and no clear relationship between the pole figures can be made,
584 unless we consider a rotation of 90° of magnetite around x, which would bring the maximum now at the S
585 to parallelism with (0001) hematite. That would imply however that, in this specific sample, we have a
586 $(100)_{mag}$ || $(001)_{hem}$ sort of relationship. Although this may represent a new possible topotactic orientation
587 relationship, one must consider that the studied EBSD map has a very large number of grains and already
588 around 40% of hematite. At these conditions, it is difficult to imagine that every single crystal of hematite
589 resulted from the transformation of magnetite on one of the symmetrically related $(111)_{mag}$ planes. I
590 believe that the transformation magnetite-hematite indeed initiates along $(111)_{mag}$ as clearly shown by
591 Barbosa and Lagoeiro (2010), but once the reaction "kicked in", hematite started to be dissolved along
592 other low index interfaces, and the initial orientation relationship was progressively lost. Deformation
593 localization in iron ores like the studied sample normally leads to the oxidation of magnetite and
594 consequent transformation to hematite, and deformation is predominantly accommodated by hematite. In
595 this case, hematite can develop stronger CPOs than magnetite (e.g., Morales et al., 2008) and that may
596 potentially affect the interphase misorientation distribution angles. It seems that in all studied cases here,

transformation from parent to daughter phase occurs preferentially (but certainly not exclusively) following certain orientation relationships.

Exploring unknown orientation relationships

So far, we have explored the interphase misorientation analysis in examples where we know that the orientation of a daughter phase is partially/completely controlled by the orientation of the parent phase. However, if one has EBSD orientation maps of "normal" rocks (polymineralic), one can explore potential interphase misorientation angle/axis relationships and find possible "orientation relationships" between the phases presented in these maps. We shall obviously not expect that all the phases will have any sort of relationship with the other phases in the aggregate, but let's us consider the example of the oxide-rich gabbro studied here. The EBSD map of this sample has 6 different minerals (plagioclase, clinopyroxene, olivine, pargasite, ilmenite and magnetite – Fig. 11 only shows the three where orientation relationships were found). Tests conducted in all possible pairs of minerals within this list resulted in 15 different interphase misorientation angle/axis pairs. From these 15 pairs, only 2 (plagioclase-olivine and plagioclase-ilmenite) have shown some sort of orientation relationships between the two phases. In both cases, the orientation relationships have nothing to do with nucleation/growth nor martensitic transformations, as the minerals have different compositions and structures. The orientation relationships between plagioclase-olivine and plagioclase-ilmenite in the studied sample seem to be related to epitaxial growth of olivine and ilmenite on plagioclase, possibly controlled by the surface energy of plagioclase and wetting surfaces on this phase.

In the studied sample, plagioclase (together with diopside) are the primary phases and crystallize first in their magmatic history, while both olivine and (later) ilmenite seem to crystallize from residual melts later in the cooling history of the gabbro. The surface energy along a solid-liquid interface is mainly controlled

623 by the atomic structure on the interface, which in turn depends on its crystal orientation (e.g., Laporte and
624 Watson, 1995). In addition, the crystallization of second phases using a host crystal as "substrate" depends
625 on the crystal structures of the two phases, and any possible relation orientation between the host and the
626 precipitate depends on the fit of the lattices between these two phases (e.g., Sutton and Balluffi, 1994). In
627 the case of the studied gabbro, the interphase misorientation axis for the pair plagioclase-ilmenite is
628 subparallel to plagioclase [100]. If we assume that the interphase misorientation axis is contained along
629 the interface, in a similar fashion as tilt grain boundaries (e.g., Lloyd. 2004), and if we assume that the
630 interface has a high tilt angle, this interface of plagioclase can have any orientation between (010) or
631 (001). From the literature, we know that the distance between the oxygen atoms connecting the SiO4 –
632 AlO4 tetrahedra in labradorite is between 4.23 and 4.26 Å , based on the determinations of Wenk et al
633 (1980). This distance is very close to the distance between O-Fe-O along the long axis of FeO_6 octahedra
634 of ilmenite, which is 4.224Å, determined by Wechsler and Prewitt (1984) and visualized with Crystal
635 Maker ®. Although plagioclase is either monoclinic or triclinic and ilmenite is trigonal, is it not
636 uncommon to find higher symmetry in certain plagioclase crystal direction. For example, plagioclase is
637 surprisingly symmetrical along [001] as noticed by Wenk et al. (2011) and Ageeva et al. (2020), Along
638 this direction, there are six-component tetrahedra "rings" that can easily accommodate the FeO_6 octahedra
639 from ilmenite. If ilmenite is then the late phase, it can crystallize using the pre-existent plagioclase as
640 substrate, where the FeO_6 octahedra are accommodated along plagioclase [001] axis by sharing some of
641 the oxygen atoms in the crystalline structure of plagioclase (substrate) with those with similar distances
642 (precipitate). Although more detail is needed and it is out of the scope of this paper, it is possible that
643 ilmenite (0001) plane and [1 0 $\bar{1}$ 0] direction of ilmenite are parallel to (120)/ ($\bar{1}$ 20) planes and [001]
644 direction of plagioclase, respectively, previously reported in Wenk et al., (2011), or one of the parallelism
645 relationships described in Ageeva et al., (2016) controls the interphase boundaries between plagioclase
646 and ilmenite.
647

As a final remark, the calculation of interphase misorientations from EBSD maps is a potential tool to, for example (i) study topotactic relationships between minerals, (ii) explore potential "orientation relationships" of different phases in a rock, (iii) to plot interphase boundaries with variable misorientation in a map, and highlight those which have special misorientation angles/axis and even possible orientation relationships and (iv) to use those maps to precisely pinpoint specific interfaces that can be further analyzed with TEM, using target preparation with focused ion beam methods for example. Steps for the calculations include (i) calculate the interphase misorientation angle distribution assuming uniform ODFs for both phases, (ii) calculate the actual correlated and uncorrelated misorientation angle distribution for the two studied phases, (iii) compare the correlated misorientation with the uncorrelated/uniform distributions in a histogram and find correlated misorientation peaks that are more frequent than those calculated for a uniform/uncorrelated distribution. After that, one can (iv) limit the misorientation angle to those higher frequent peaks of any range and then plot those in inverse pole figures of combined crystal symmetries and (v) plot the different range of interphase misorientations directly on EBSD maps. If for example topotactic relationships exist between the two phases, one can calculate what is the pair misorientation angle/axis pair for such a relation, and look into an EBSD map for the presence of these relationships, based on a misorientation angle range that includes the specific misorientation angle for the specific topotactic relationship.

ACKNOWLEDGEMENTS

I would like to thanks Sebastian Cionoiu and Lucie Tajcmanova for the calcite-aragonite sample, and Jessica Till for the gabbro sample. I am also grateful for the detailed reviews by Luca Menegon and the anonymous reviewer, which improved considerably the quality of the paper, and by the editorial handling and the tedious work of correcting my English by Dr. Sergio Speziale.

REFERENCES CITED

Ageeva O, Habler G, Topa D, Waitz T, Li C, Pertsev A, Zhilicheva O, Abart R (2016) Plagioclase hosted Fe-Ti-oxide micro-inclusions in an oceanic gabbro-plagiogranite association from the Mid Atlantic Ridge at 13° 34' N. American Journal of Science 316:85–109

Ageeva, O., Bian, G., Habler, G., Pertsev, A., Abart, R. (2020). Crystallographic and shape orientations of magnetite micro-inclusions in plagioclase, Contributions to Mineralogy and Petrology 175: 95, 020) 175:95, doi.org/10.1007/s00410-020-01735-8.

Alkmim, F., Marshak, S., (1998) Transamazonian orogeny in the southern São Francisco craton region, Minas Gerais, Brazil: evidence for Paleoproterozoic collision and collapse in the Quadrilátero Ferrífero. Precambrian Research 90, 29–58.

Barbosa, P. F., Lagoeiro, L.E. (2010). Crystallographic texture of the magnetite-hematite transformation: Evidence for topotactic relationships in natural samples from Quadrilátero Ferrífero, Brazil. American Mineralogist 95, 118-125.

Bestmann, M.; Prior, D.J. (2003). Intragranular dynamic recrystallization in naturally deformed calcite marble: diffusion accommodated grain boundary sliding as a result of subgrain rotation recrystallization. Journal of Structural Geology 25, 1597-1613

Boudier, F., Baronnet, A., Mainprice, D. (2010). Serpentine mineral replacements of natural olivine and their seismic implications: oceanic lizardite versus subduction-related antigorite. Journal of Petrology 51 (1–2), 495–512, http://dx.doi.org/10.1093/petrology/egp049.

Carlson, W.D., Rosenfeld, J.L. (1981) Optical determination of topotactic aragonite-calcite growth kinetics: metamorphic implications. Journal of Geology 89, 615-638

Cionoiu, S. (2019). Experimental and Numerical Predictions of Phase Transitions in Solids under Differential Stress. PhD Thesis, ETH Zürich. https://doi.org/10.3929/ethz-b-000353445

Duyster, J., Stöckhert, B. (2001) Grain boundary energies in olivine derived from natural microstructures. Contributions to Mineralogy and Petrology 140 (5), 567-576.

Faul, U.H., Fitz-Gerald, J. (1999) Grain misorientations in partially molten olivine aggregates: an electron backscatter diffraction study. Contributions to Mineralogy and Petrology 26, 187-197

Gillet, P., Gerard, Y., Williame, C. (1987) The calcite-aragonite transition: mechanism and microstructure induced by transformation stresses and strain. Bulletin de sMinéralogie 110, 481-496.

Guillet, P., Madon, M., (1982) Un modèle de dislocations pour la transition aragonite-calcite. Bulletin de Minéralogie 105, 590-597.

Hielscher, R., Schaeben, H. (2008) A novel pole figure inversion method: specification of the MTEX algorithm. Journal of Applied Crystallography 41, 1024–1037. http://dx.doi.org/10.1107/S0021889808030112.

Hiraga, T., Anderson, I. M., Kohlstedt, D. L. (2004) Grain boundaries as reservoirs of incompatible elements in the Earth's mantle. Nature 427, 699-703

725 Hunter, W.C., Smith, D. (1981) Garnet peridotite from Colorado Plateau ultramafic diatremes: hydrates,
726 carbonates and comparative geothermometry. Contributions to Mineralogy and Petrology 76, 312–320.
727
728 Karson, J. A., Lawrence, R. M. (1997) Tectonic window into gabbroic rocks of the middle oceanic crust in
729 the MARK area near Sites 921–924, Proceeding of the Ocean Drilling Program Scientific Results, 153,
730 61–76, doi:10.2973/odp.proc.sr.153.005.1997.
731
732 Kelemen, P. B., Kikawa, E., Miller, D. J. and the Shipboard Scientific Party (2007), Leg 209 summary:
733 Processes in a 20- km-thick conductive boundary layer beneath the Mid-Atlantic Ridge, 14_–16_N, Proc.
734 Ocean Drill. Program Sci. Results, 209, 1–33, doi:10.2973/odp.proc.sr.209.001.2007.
735
736 Kilian, R., Heilbronner, R., and Stunitz, H. (2011). Quartz grain size reduction in a granitoid rock and the
737 transition from dislocation to diffusion creep. Journal of Structural Geology 33, 1265–1284,
738 https://doi.org/10.1016/j.jsg.2011.05.004
739
740 Krakow, R., Bennet, R.B., Johnstone, D.N., Vukmanovic, Z., Solano-Alvares, W., Laine, S.J.,Einsle, J.F.,
741 Midgley, P., Rae, C., Hielscher, R. (2017) On three-dimensional misorientation spaces. Proceedings of the
742 Royal Society A 473: 20170274. http://dx.doi.org/10.1098/rspa.2017.0274
743
744 Kruhl, J., Wirth, R., Morales, L.F.G. (2013) Quartz grain boundaries as fluid pathways in metamorphic
745 rocks. Journal of Geophysical Research Vol. 118(5), 1957–1967. doi:10.1029/2012JB009644
746
747 Lagoeiro, L.E. 1998. Transformation of magnetite to hematite and its influence on the dissolution of iron
748 oxide minerals. Journal of Metamorphic Petrology 16, 415-423
749

Laporte, D., Watson, E. B. (1995) Experimental and theoretical constraints on melt distribution in crustal sources: The effect of crystalline anisotropy on melt interconnectivity, Chemical Geology 124, 161–184, doi:10.1016/0009-2541(95)00052-N.

Lloyd G.E., Farmer A.B., Mainprice, D. (1997) Misorientation analysis and the formation and orientation of subgrain and grain boundaries. Tectonophysics 279, 55-78.

Lloyd, G. E. (2004) Microstructural evolution in a mylonitic quartz simple shear zone: the significant roles of dauphine twinning and misorientation. In: Alsop, G. I., Holdsworth, R. E., McCaffrey, K. & Handy, M. (eds) Transports and Flow Processes in Shear Zones. Geological Society, London, Special Publications, 224, 39–61.

Mainprice, D., Humbert, M., Wagner, F. 1990. Phase transformations and inherited lattice preferred orientations: implications for seismic properties. Tectonophysics 180, 213-218.

Mainprice, D., Lloyd, G.E., Casey, M. (1993) Individual orientation measurements in quartz polycrystals - advantages and limitations for texture and petrophysical property determinations. Journal of Structural Geology 15, 1169-1187

Marquardt, K., Rohrer, G.S., Morales, L., Rybacki, E., Marquardt, H.; Lin, B. (2015). The most frequent interfaces in olivine aggregates: The GBCD and its importance for grain boundary related processes. Contributions to Mineralogy and Petrology 170:40, doi: 10.1007/s00410-015-1193-9.

Marti, S., Stünitz, H., Heilbronner, R., Plümper, O., Kilian, R. (2018) Syn-kinematic hydration reactions, grain size reduction, and dissolution–precipitation creep in experimentally deformed plagioclase–pyroxene mixtures. Solid Earth, 9, 985–1009 https://doi.org/10.5194/se-9-985-2018

McGetchin, T.R., Silver, L.T. (1970) Compositional relations in minerals from kimberliticand related rocks in the Moses Rock Dike, San Juan County, Utah. American Mineralogist 55, 1738–1771.

McLaren, A. C. (1986) Some speculations on the nature of high angle grain boundaries in quartz rocks, in Mineral and Rock Deformation: Laboratory Studies: The Paterson Volume, pp. 233–245, AGU, Washington, D. C.

McNamara, D. D., Wheeler, J., Pearce, M., & Prior, D. J. (2012). Fabrics produced mimetically during static metamorphism in retrogressed eclogites from the Zermatt-Saas zone, Western Italian Alps. Journal of Structural Geology 44, 167-178. http://dx.doi.org/10.1016/j.jsg.2012.08.006

McTigue Jr., J.W., Wenk, H.-R. (1985) Microstructure and orientation relationships in the dry-state aragonite-calcite and calcite-lime phase transformations. American Mineralogist 70, 1253-1261

Menegon, L., Nasipuri, P., Stünitz, H., Behrens, H., Ravna, E. (2011). Dry and strong quartz during deformation of the lower crust in the presence of melt. Journal of Geophysical Research 116, B10410. http://dx.doi.org/10.1029/2011JB008371.

Menegon, L., Piazolo, S., Pennacchioni, G. (2010). The effect of Dauphiné twinning on plastic strain in quartz. Contributions to Mineralogy and Petrology. 161, 635–652.

Miranda, E.A., John, B.E. (2010) Strain localization along the Atlantis Bank oceanic detachment fault system, Southwest Indian Ridge. Geochemistry, Geophysics, Geosystems 11(4), doi:10.1029/2009GC002646

801 Morales, L.F.G., Mainprice, D., Boudier, F. (2013) The influence of hydrous phase on the microstructure
802 and seismic properties of a hydrated mantle rock. Tectonophysics 594, 103–117.
803
804 Morales, L.F.G., Mainprice, D., Kern, H. (2018) Olivine-antigorite orientation relationships:
805 microstructures, phase boundary misorientation and seismic properties. Tectonophysics 724-725, 93-115.
806
807 Morawiec A (1997) Distributions of misorientation angles and misorientation axes for crystallites with
808 different symmetries. Acta Crystallographica A53, 273-285
809
810 Morawiec, A. (1995) Misorientation angle distribution of randomly oriented symmetric objects. Journal of
811 Applied Crystallography 28, 289-293
812
813 Obata, M, Ozawa, K. (2011) Topotaxic relationships between spinel and pyroxene in kelyphite after
814 garnet in mantle-derived peridotites and their implications to reaction mechanism and kinetics.
815 Mineralogy and Petrology 101, 217-224, doi:10.1007/s00710-011-0145-y
816
817 Plümper, O., King, H.E., Vollmer, C., Ramasse, Q., Jung, H., Austrheim, H. (2012) The legacy of crystal-
818 plastic deformation in olivine - high-diffusivity pathways during serpentinization. Contribution to
819 Mineralogy and Petrology 163 (4), 701–724.
820
821 Porter, D.A., Easterling, K.E. (1992). Phase transformations in metals and alloys. Chapmann and Hall
822
823 Rosière, C.A., Siemes, H., Quade, H., Brokmeier, H.G., Jansen, E.M. (2001) Microstructures, textures and
824 deformation mechanisms in hematite. Journal of Structural Geology 23, 1429–1440.
825

826 Smith, D. (1995) Chlorite-rich ultramafic reaction zones in Colorado Plateau xenoliths: recorders of sub-
827 Moho hydration. Contributions to Mineralogy and Petrology 121, 185–200.
828
829 Smith, D. (2010). Antigorite peridotite, metaserpentinite, and other inclusions within diatremes on the
830 Colorado Plateau, SW USA: implications for the mantle wedge during low-angle subduction. Journal of
831 Petrology 51 (6), 1355–1379.
832
833 Sutton A.P., Balluffi, R.W. (1995) Interfaces in Crystalline Materials. Clarendon Press, Oxford, UK
834
835 Wenk, H.-R., Janssen, C., Kenkmann, T., Dresen, G. (2011) Mechanical twinning in quartz: Shock
836 experiments, impact, pseudotachylites and fault breccias. Tectonophysics 510, 59-79
837
838 Wenk HR, Chen K, Smith R (2011) Morphology and microstructure of magnetite and ilmenite inclusions
839 in plagioclase from Adirondack anorthositic gneiss. American Mineralogist 96(8–9):1316–1324
840
841 Wheeler, J., Prior, D.J., Jiang, Z., Speiss, R., & Trimby, P.W. (2001). The petrological significance of
842 misorientations between grains. Contributions to Mineralogy and Petrology 141, 109-124.
843
844 **FIGURE CAPTIONS**
845
846 **Figure 1** – Schematic drawing showing the misorientation between 2 different phases, one "hexagonal"
847 (yellow grain) and a second, "cubic" (purple and green grains). The orientation of the individual
848 crystallites is described by an orientation $\mathbf{g_1}$, $\mathbf{g_2}$ or $\mathbf{g_3}$, which describes the transformation from crystal
849 reference frame (c_i) and sample reference frame (r), here denoted as x,y and z. The misorientation (M)
850 between grains of the same phase can be described as $M=\mathbf{g_2}^{-1}\mathbf{g_3}$, where g are their respective orientations.
851 The misorientation along different phases nevertheless ($M(ip)$ needs to consider the crystallographic

system of the individual phases (*cs*), and can be described like $\boldsymbol{M(ip)}=\mathbf{g}_{\mathbf{1}(cs1)}^{-1}\,\mathbf{g}_{\mathbf{3}(cs2)}$, where cs_1 is the crystal symmetry of phase 1 (e.g. hexagonal) and cs_2 the crystal symmetry of phase 2 (e.g. cubic). The combined symmetries of the different cs is what defines the dimensions of the fundamental zones for the plots presented here.

Figure 2 – (a) Combined phase and image quality map, showing the distribution of calcite and aragonite. Orientation maps for calcite and aragonite, respectively, inverse pole figure color-coded.

Figure 3 – Pole figures for calcite and aragonite considering all points in the orientation maps from Fig. 2. Scale is given in multiples of uniform distribution. ODFs calculated assuming a halfwidth of 10°.

Figure 4 – Interphase misorientation angle (a) and axis (b) distribution for calcite-aragonite, assuming a uniform distribution function, with calcite reference frame plotted in (b). Interphase misorientation angle distribution (c) as calculated from the EBSD orientation map. Red bars on the histogram show the correlated misorientation (between neighbor grains), the orange curve shows the uncorrelated distribution calculated from the orientation distribution function, and the yellow curve shows the uniform misorientation angle distribution as in (a). Correlated interphase misorientation axis distribution plotted against the calcite reference frame, for all range of misorientation axes from (c). (e) Phase map showing calcite (purple) and aragonite (green), and the more common interphase boundaries traces, with misorientations between adjacent crystals ranging from 30 to 70°. Scales in the pole figures b and d are given in multiples of uniform distribution.

Figure 5 – (a) Combined phase and image quality map, showing the distribution of olivine (purple) and antigorite (green), whereas the red phase at the top right and bottom left are isolated grains of magnetite.

877 **Figure 6** - Pole figures for olivine and antigorite, considering all points in the orientation maps from Fig.
878 5. Scale is given in multiples of uniform distribution. ODFs calculated assuming a halfwidth of 10°.
879
880 **Figure 7** - Interphase misorientation angle (a) and axis (b) distribution for olivine-antigorite, assuming a
881 uniform distribution function, with olivine reference frame plotted in (b). Interphase misorientation angle
882 distribution (c) as calculated from the EBSD orientation map. Red bars on the histogram show the
883 correlated misorientation (between neighbor grains), the orange curve shows the uncorrelated distribution
884 calculated from the misorientation distribution function, and the yellow curve shows the uniform
885 misorientation angle distribution as in (a). Correlated interphase misorientation axis distribution (d)
886 plotted against the olivine reference frame, for misorientations ranging from 70-100°. (e) Image quality
887 map showing the more common interphase boundaries, with misorientations ranging from 70 to 100°.
888 Scales in the pole figures b and d are given in multiples of uniform distribution. The phase map is not
889 presented here for better visualization of the interfaces.
890
891 **Figure 8** - (a) Combined phase and image quality map, showing the distribution of magnetite (purple) and
892 hematite (green).
893
894 **Figure 9** - Pole figures for magnetite and hematite, considering all points in the orientation maps from
895 Fig. 8. Scale is given in multiples of uniform distribution. ODFs calculated assuming a halfwidth of 10°.
896
897 **Figure 10** - Interphase misorientation angle (a) and axis (b) distribution for magnetite and hematite,
898 assuming a uniform distribution function, with magnetite reference frame plotted in (b). Interphase
899 misorientation angle distribution (c) as calculated from the EBSD orientation map. Red bars on the
900 histogram show the correlated misorientation (between neighbor grains), the orange curve shows the
901 uncorrelated distribution calculated from the misorientation distribution function, and the yellow curve
902 shows the uniform misorientation angle distribution as in (a). Correlated interphase misorientation axis

903 distribution (d) plotted against the magnetite reference frame, for misorientations ranging from 20-50°. (e)
904 Image quality (IQ) map showing the most common interphase boundaries traces with misorientations
905 between adjacent grains ranging from 20 to 50°. Scales in the pole figures b and d are given in multiples
906 of uniform distribution. The phase map is not presented here for better visualization of the interfaces.
907
908 **Figure 11** - (a) Combined phase and image quality map, showing the distribution of plagioclase (green),
909 olivine (red) and ilmenite (blue) in the studied gabbro sample. (b) Combined orientation map for
910 plagioclase (IPF color-coded) and image quality for the rest of the phases.
911
912 **Figure 12** - Pole figures for plagioclase, olivine and ilmenite, considering all points in the orientation
913 maps from Fig. 8. Scale is given in multiples of uniform distribution. ODFs calculated assuming a
914 halfwidth of 10°.
915
916 **Figure 13** - Interphase misorientation angle (a, c) and axis (b, d) distribution for the pairs plagioclase-
917 olivine and plagioclase-ilmenite, respectively, assuming a uniform orientation distribution function. On
918 stereogram (b) plagioclase reference frame is given as black letters in white background, whereas certain
919 olivine directions are given in black background and white letters. The same is valid for the plot (d), but
920 for ilmenite. Scale bars in b and d are given in multiples of uniform distribution.
921
922 **Figure 14** - Interphase misorientation angle distribution (a, c) and axes (b, d) as calculated from the EBSD
923 orientation map, for the pairs plagioclase-olivine and plagioclase-ilmenite, respectively. Red bars on the
924 histogram show the correlated misorientation (between neighbor grains), the orange curve shows the
925 uncorrelated distribution calculated from the misorientation distribution function, and the yellow curve
926 shows the uniform misorientation angle distribution as in Fig. 13 a,c. On the plot (b) misorientation angles
927 are limited to a range between 65-90° for plagioclase-olivine, whereas in (d) the misorientation range is
928 from 85-130°, for plagioclase-ilmenite pair. On stereogram (b) plagioclase reference frame is given as

929 black letters in white background, whereas certain olivine directions are given in black background and
930 white letters. The same is valid for the plot (d), but for ilmenite. Scale bars in b and d are given in
931 multiples of uniform distribution.
932
933 **Figure 15** – Image quality maps showing plagioclase-olivine interphase boundaries traces with adjacent
934 interphase misorientations ranging from 60-100° misorientation (a) and plagioclase-ilmenite interface
935 traces with misorientation ranging from 60-120°.
936

This is the peer-reviewed, final accepted version for American Mineralogist, published by the Mineralogical Society of America.
The published version is subject to change. Cite as Authors (Year) Title. American Mineralogist, in press.
DOI: https://doi.org/10.2138/am-2021-7902. http://www.minsocam.org/

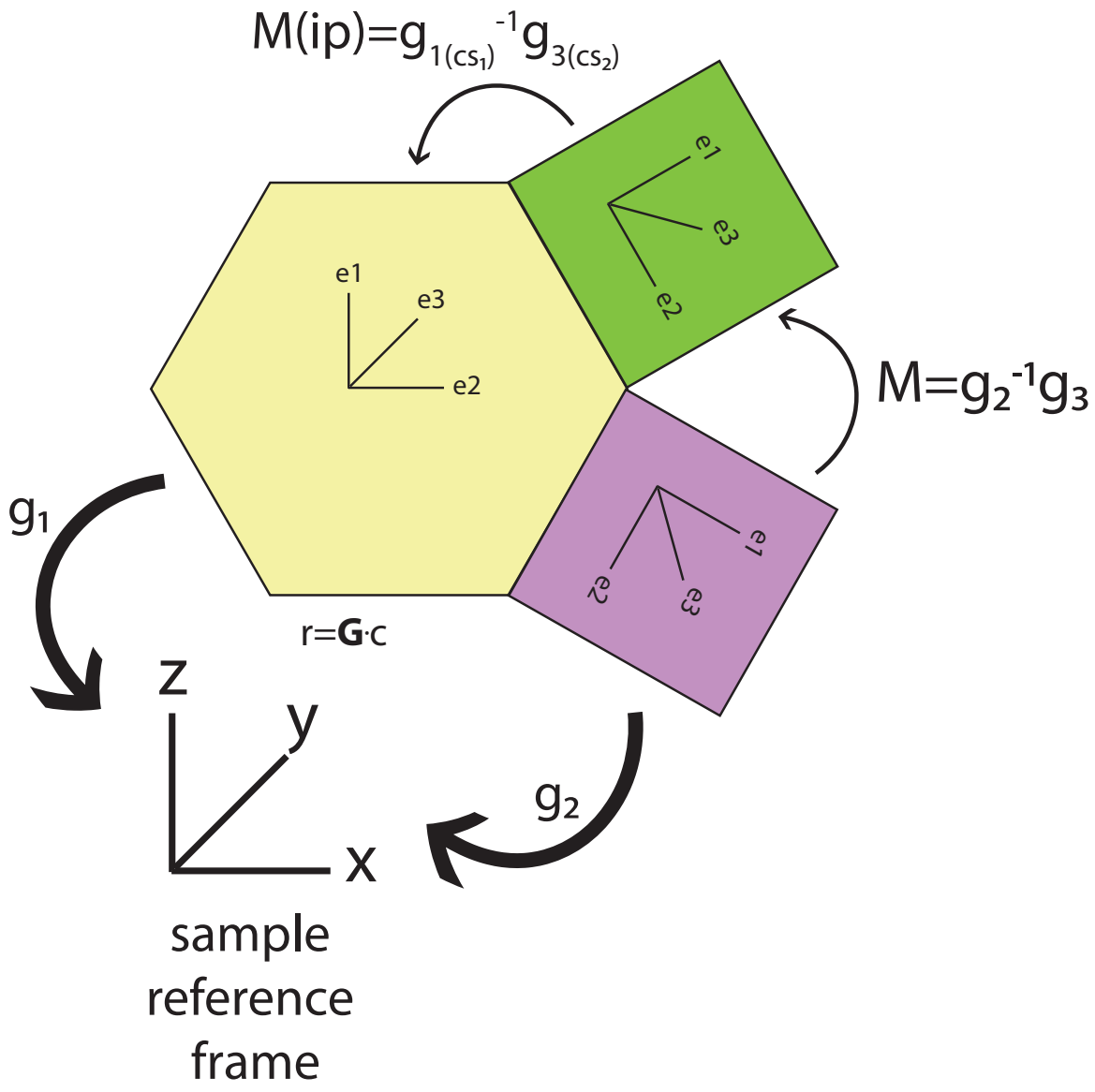

Figure 1

This is the peer-reviewed, final accepted version for American Mineralogist, published by the Mineralogical Society of America.
The published version is subject to change. Cite as Authors (Year) Title. American Mineralogist, in press.
DOI: https://doi.org/10.2138/am-2021-7902. http://www.minsocam.org/

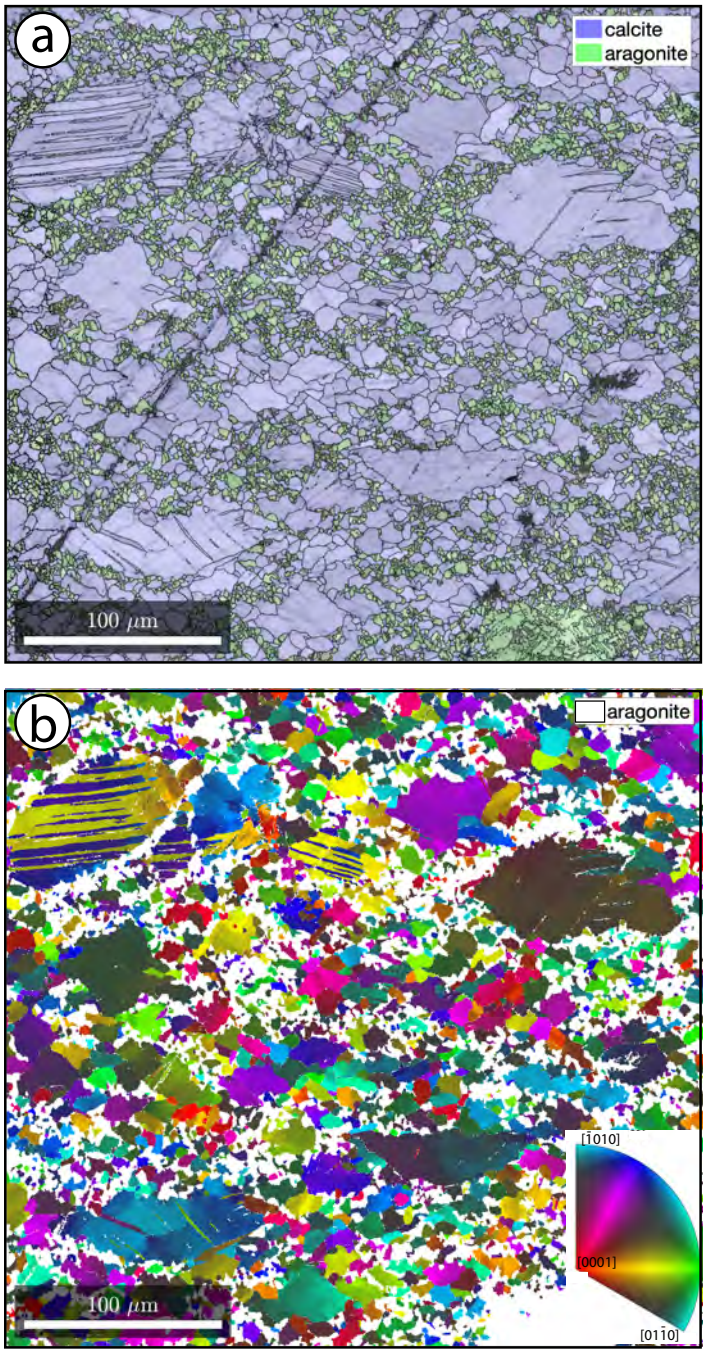

Figure 2

This is the peer-reviewed, final accepted version for American Mineralogist, published by the Mineralogical Society of America.
The published version is subject to change. Cite as Authors (Year) Title. American Mineralogist, in press.
DOI: https://doi.org/10.2138/am-2021-7902. http://www.minsocam.org/

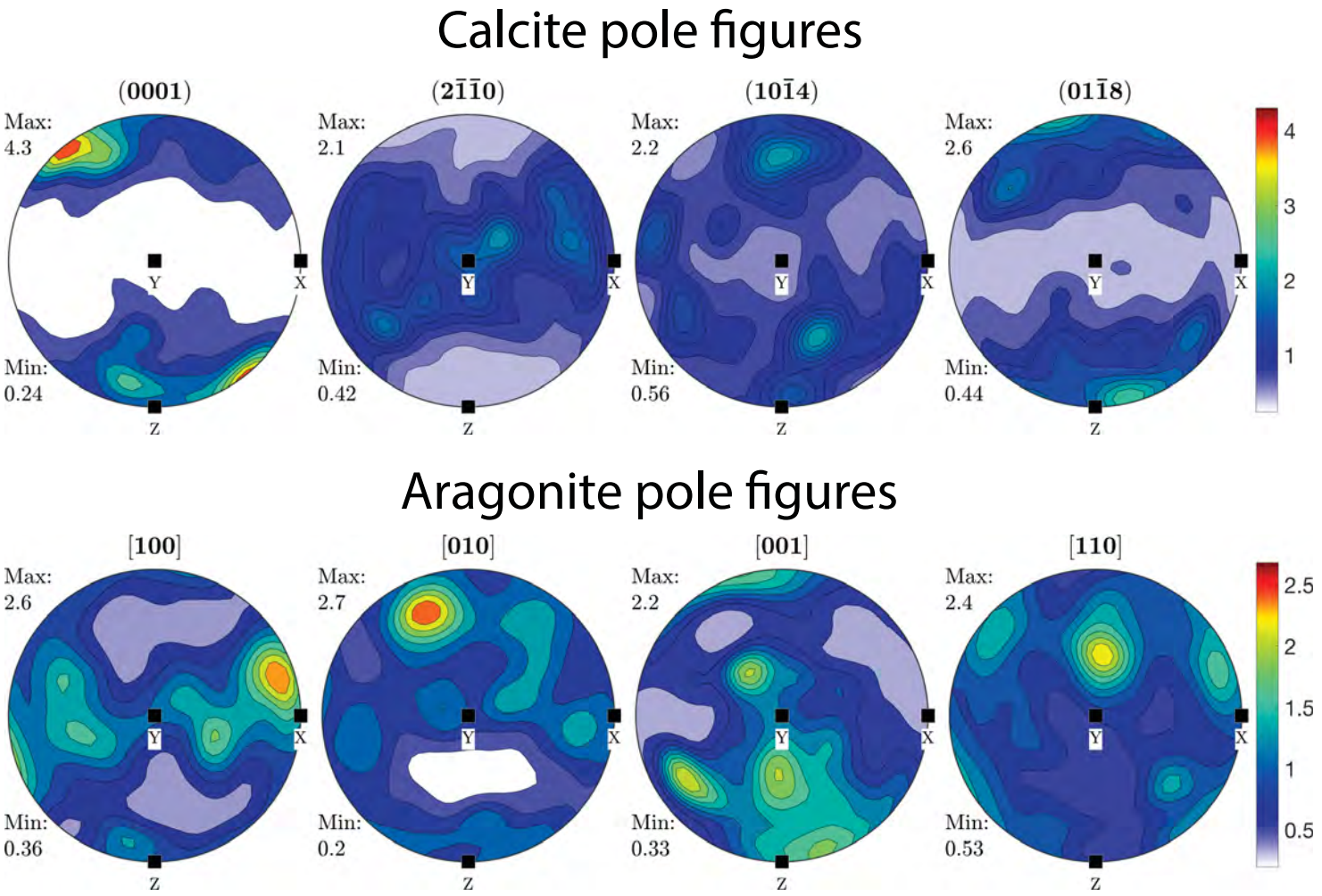

Figure 3

This is the peer-reviewed, final accepted version for American Mineralogist, published by the Mineralogical Society of America.
The published version is subject to change. Cite as Authors (Year) Title. American Mineralogist, in press.
DOI: https://doi.org/10.2138/am-2021-7902. http://www.minsocam.org/

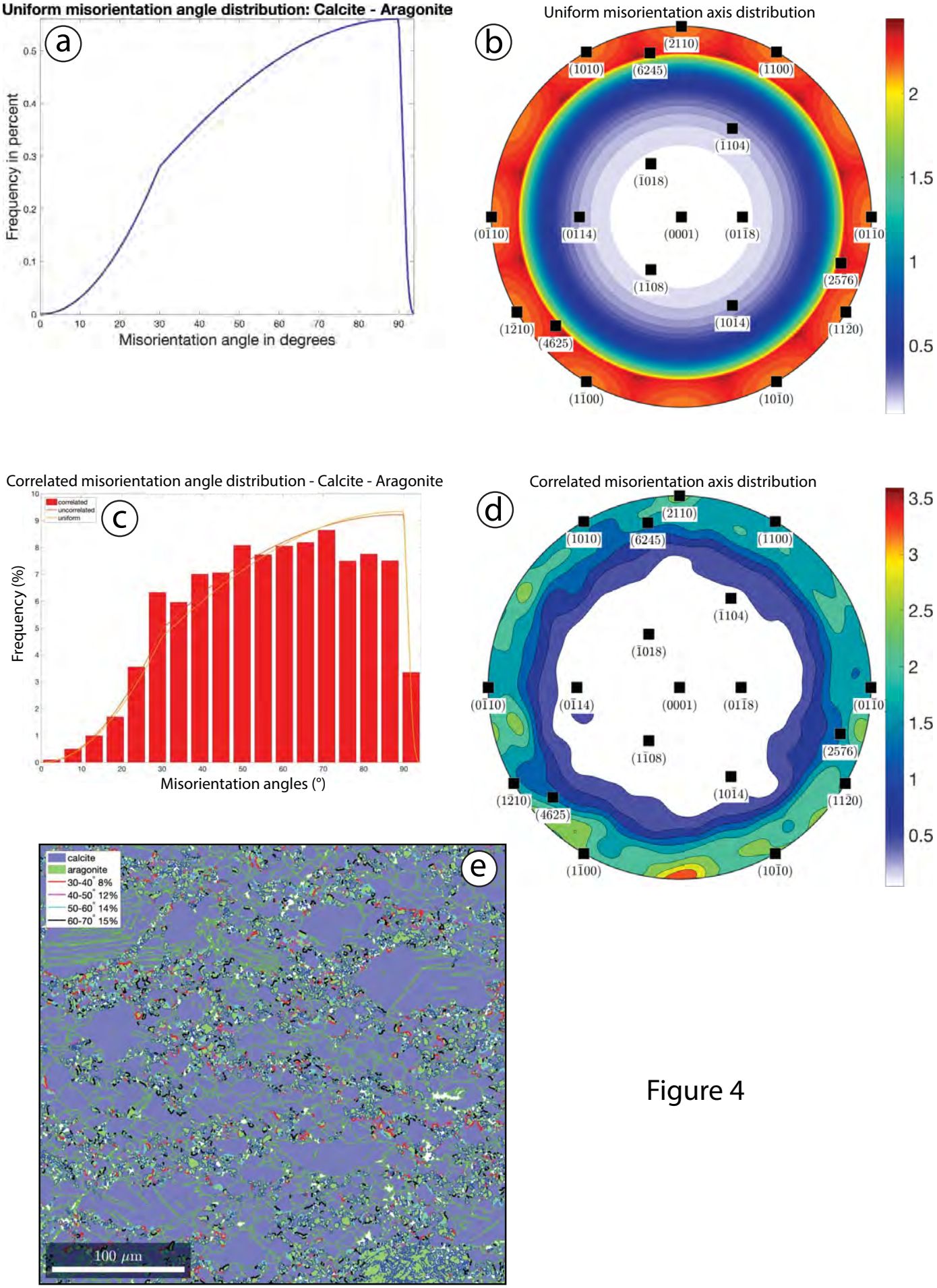

Figure 4

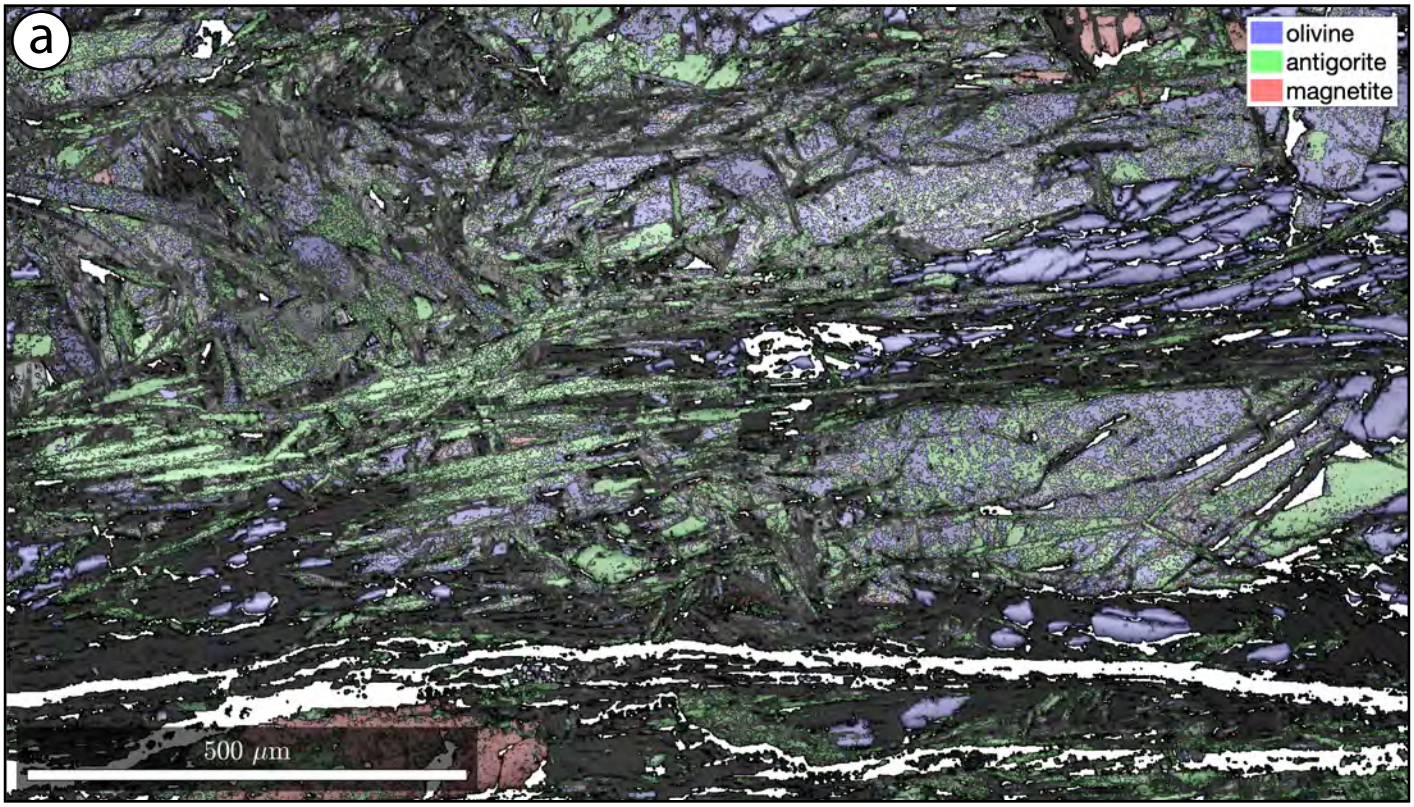

Figure 5

This is the peer-reviewed, final accepted version for American Mineralogist, published by the Mineralogical Society of America.
The published version is subject to change. Cite as Authors (Year) Title. American Mineralogist, in press.
DOI: https://doi.org/10.2138/am-2021-7902. http://www.minsocam.org/

Olivine pole figures

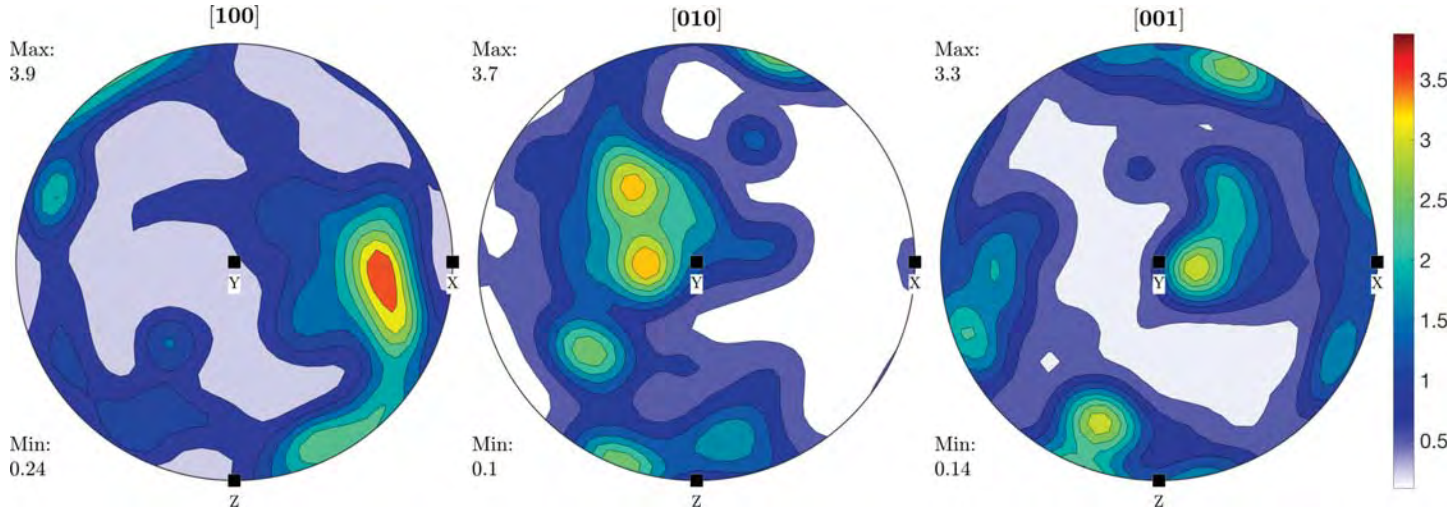

Antigorite pole figures

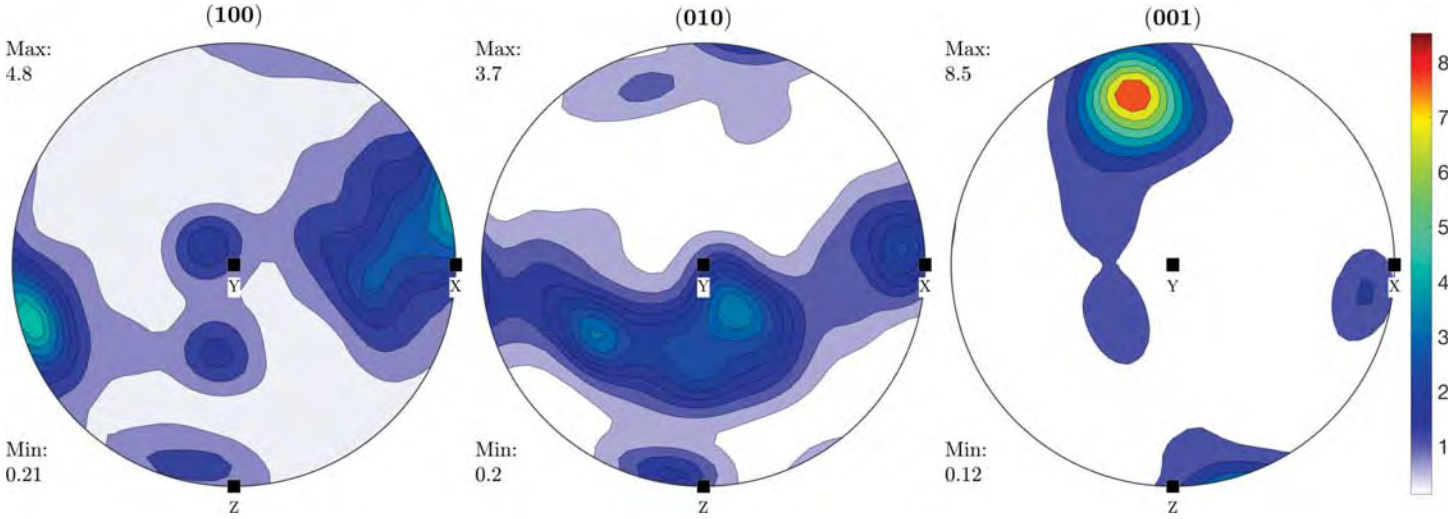

Figure 6

This is the peer-reviewed, final accepted version for American Mineralogist, published by the Mineralogical Society of America.
The published version is subject to change. Cite as Authors (Year) Title. American Mineralogist, in press.
DOI: https://doi.org/10.2138/am-2021-7902. http://www.minsocam.org/

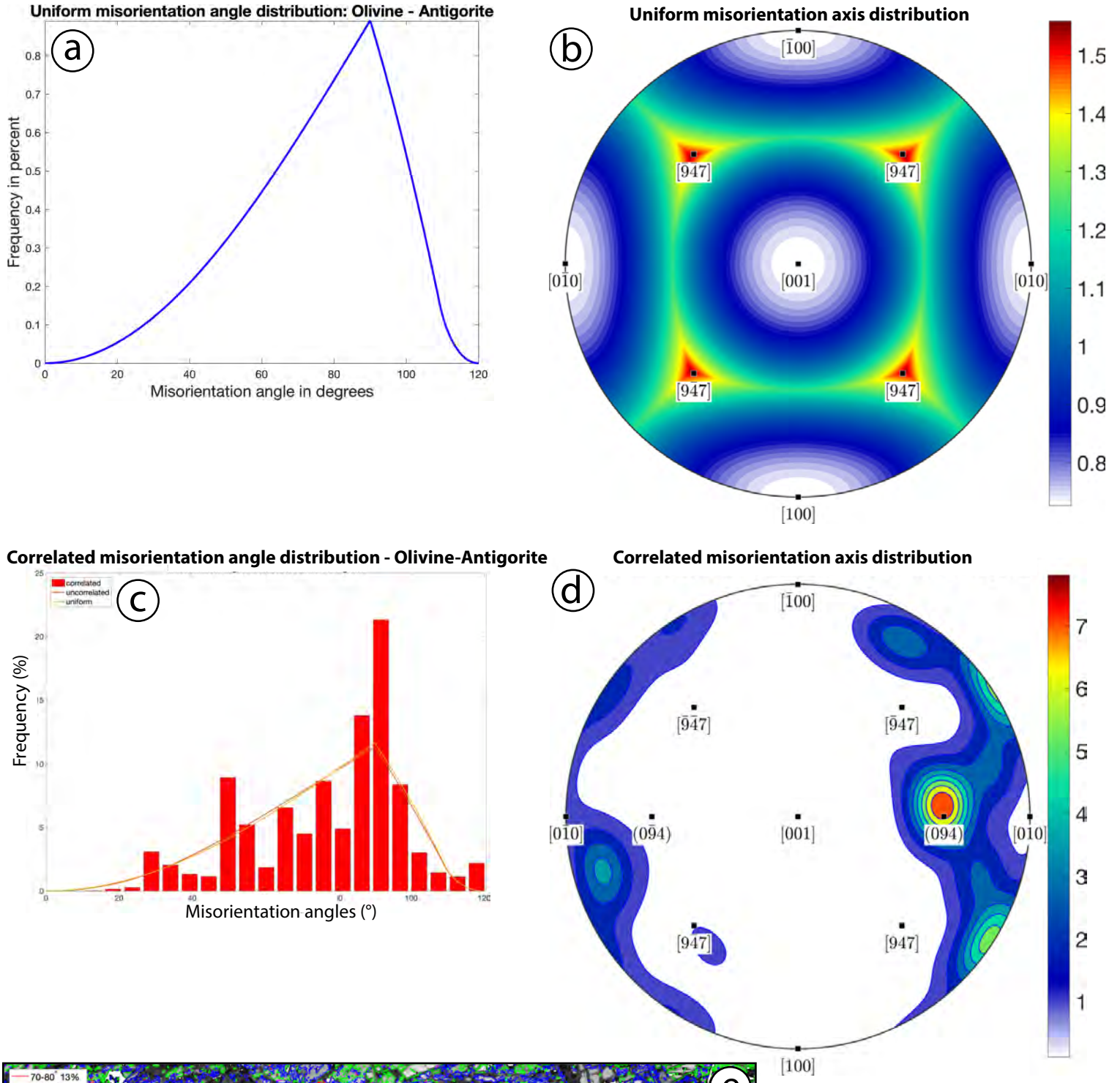

Figure 7

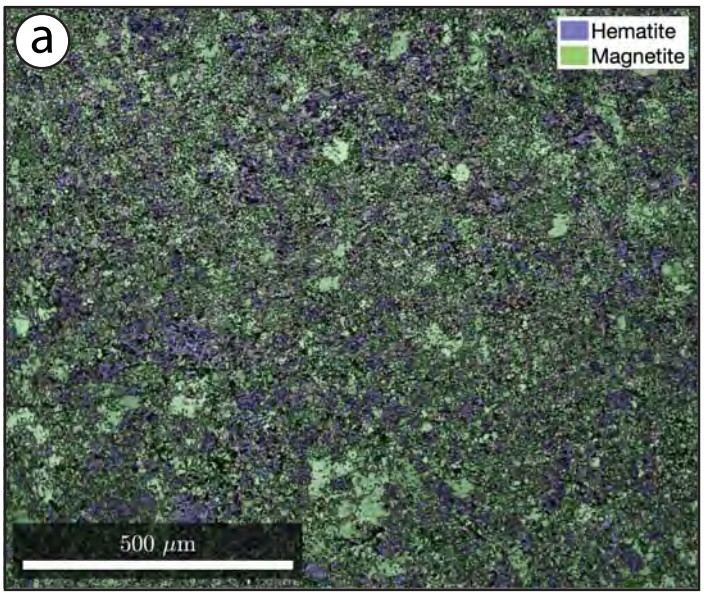

Figure 8

This is the peer-reviewed, final accepted version for American Mineralogist, published by the Mineralogical Society of America.
The published version is subject to change. Cite as Authors (Year) Title. American Mineralogist, in press.
DOI: https://doi.org/10.2138/am-2021-7902. http://www.minsocam.org/

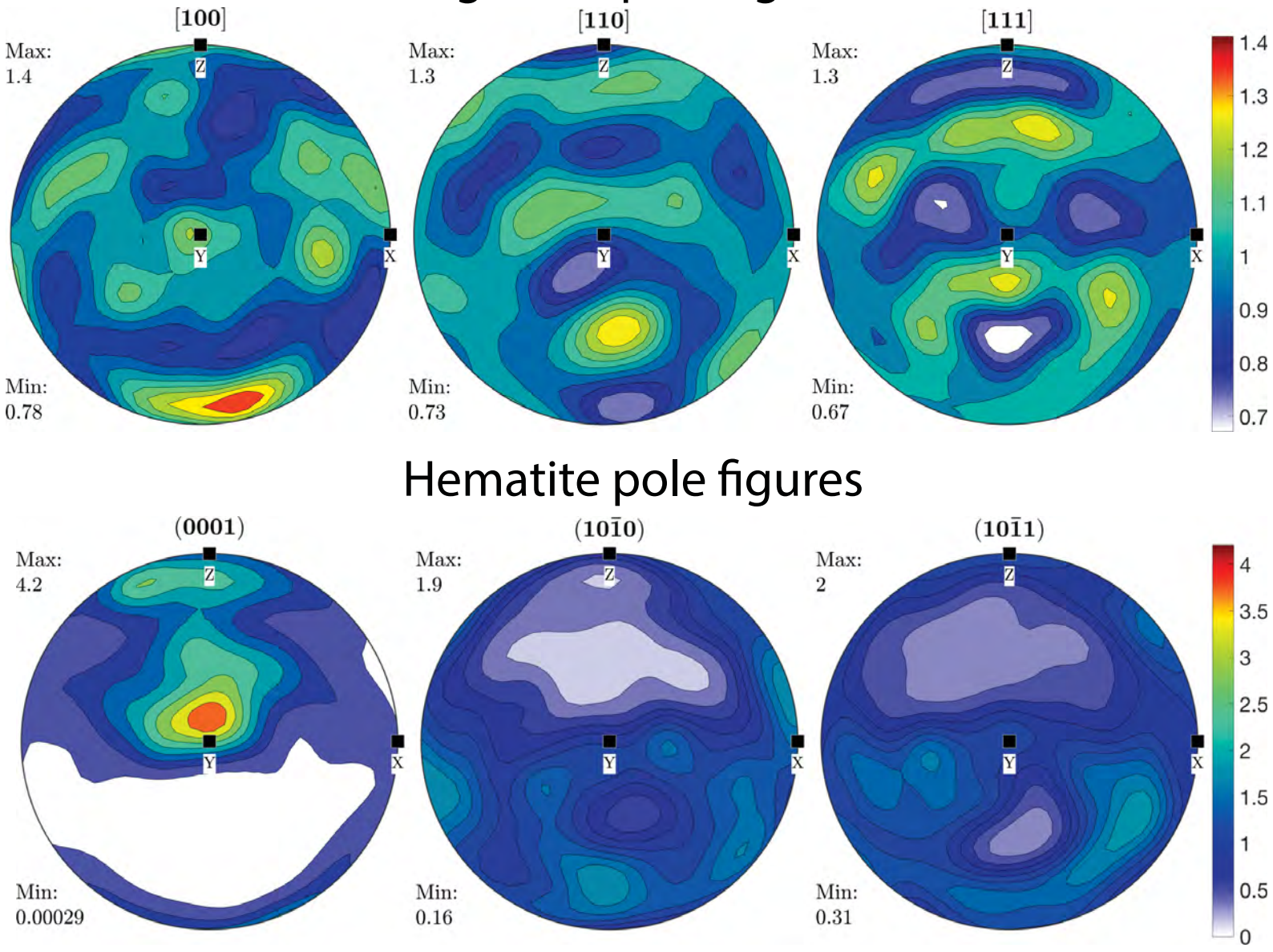

Figure 9

This is the peer-reviewed, final accepted version for American Mineralogist, published by the Mineralogical Society of America.
The published version is subject to change. Cite as Authors (Year) Title. American Mineralogist, in press.
DOI: https://doi.org/10.2138/am-2021-7902. http://www.minsocam.org/

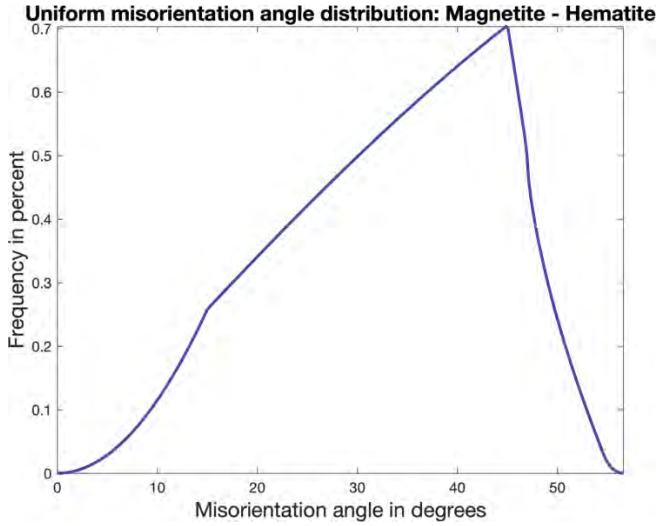

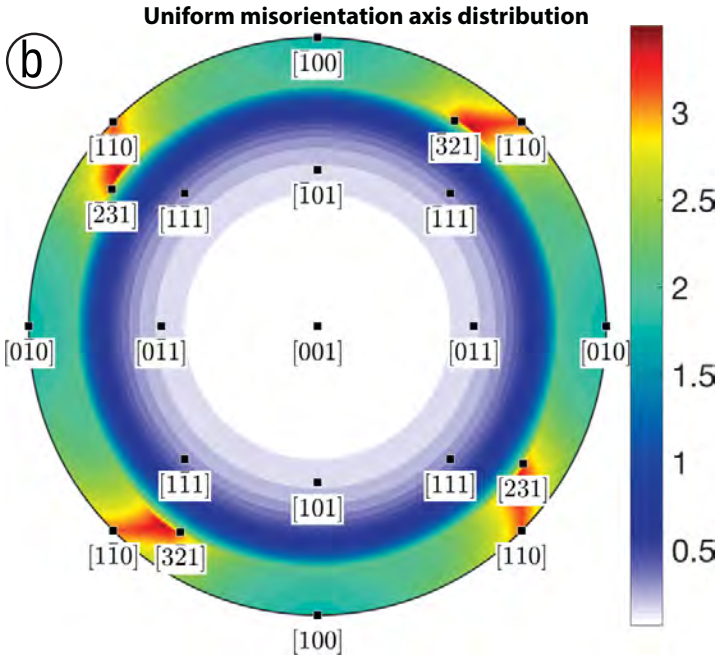

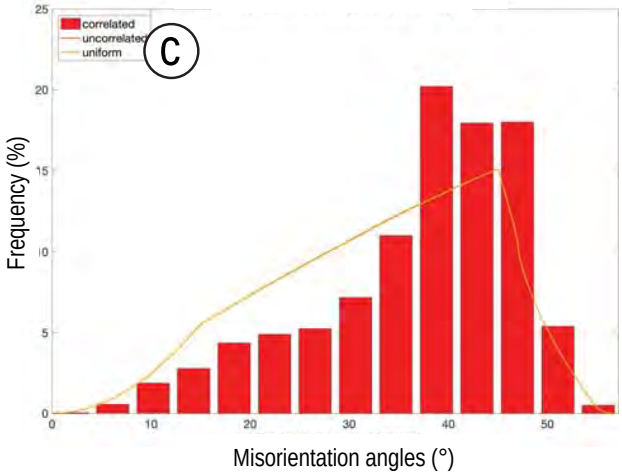

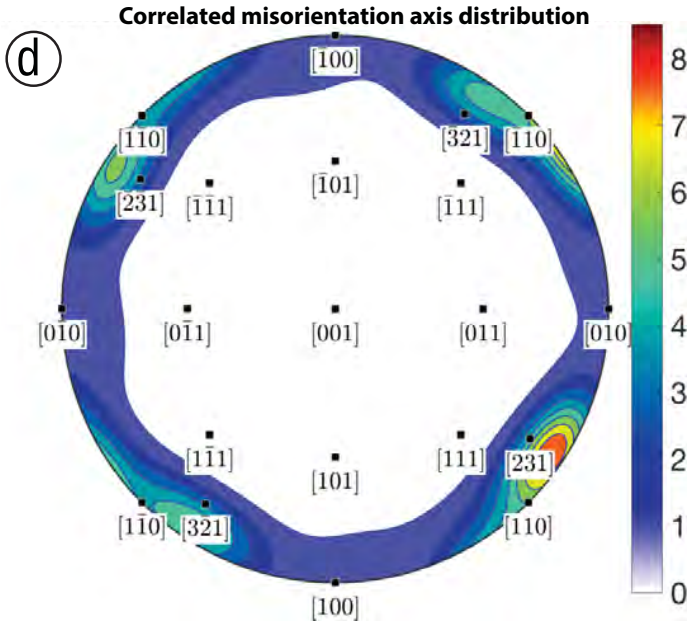

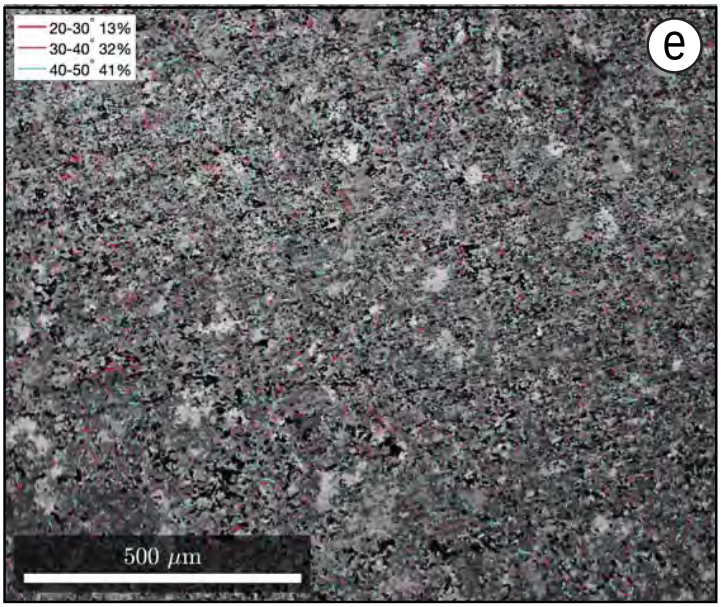

Figure 10

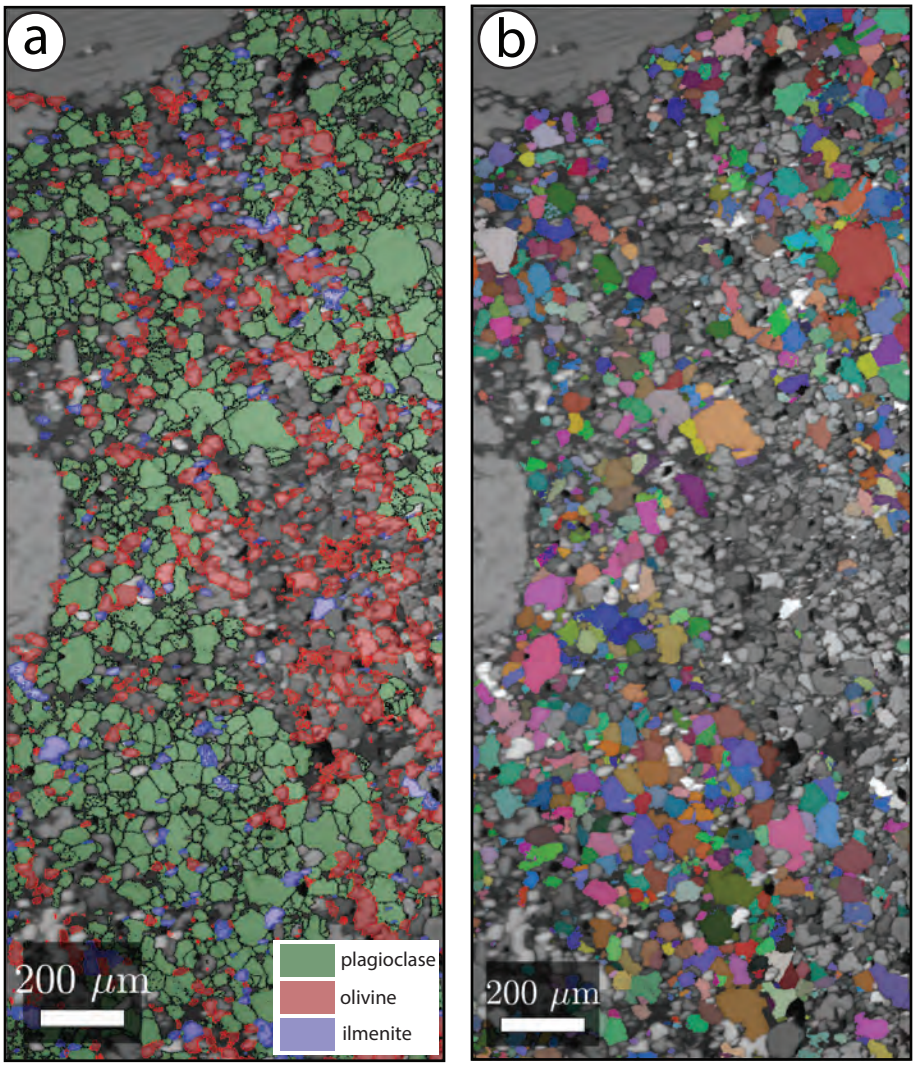

Figure 11

This is the peer-reviewed, final accepted version for American Mineralogist, published by the Mineralogical Society of America.
The published version is subject to change. Cite as Authors (Year) Title. American Mineralogist, in press.
DOI: https://doi.org/10.2138/am-2021-7902. http://www.minsocam.org/

Plagioclase pole figures

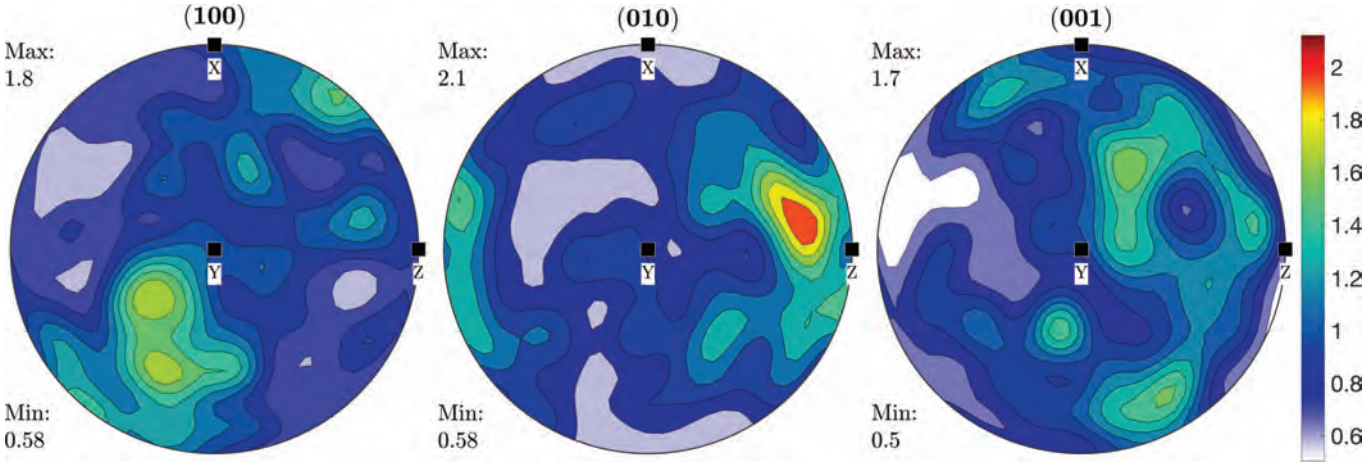

Olivine pole figures

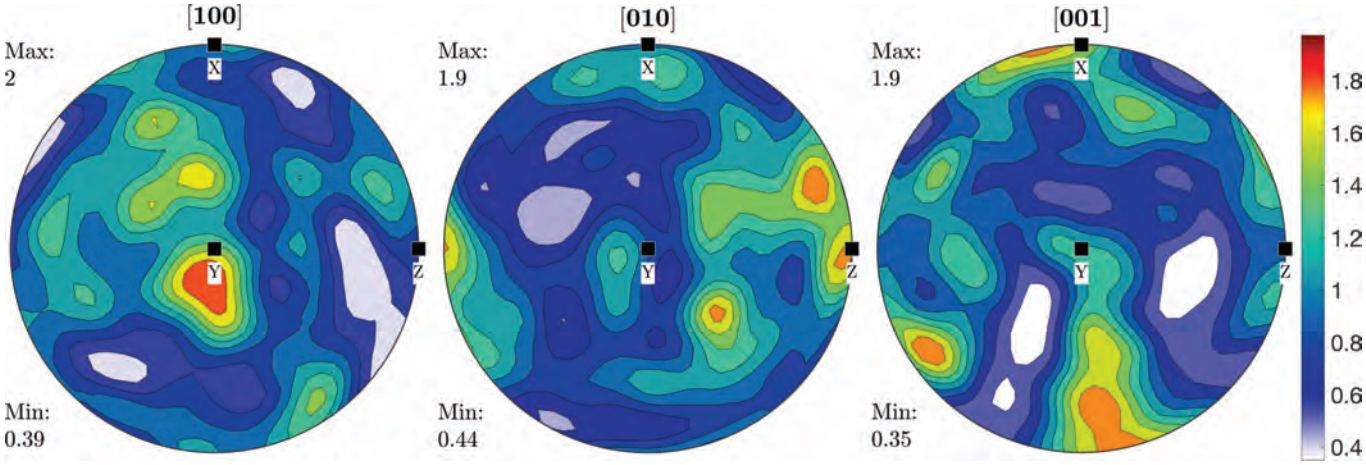

Ilmenite pole figures

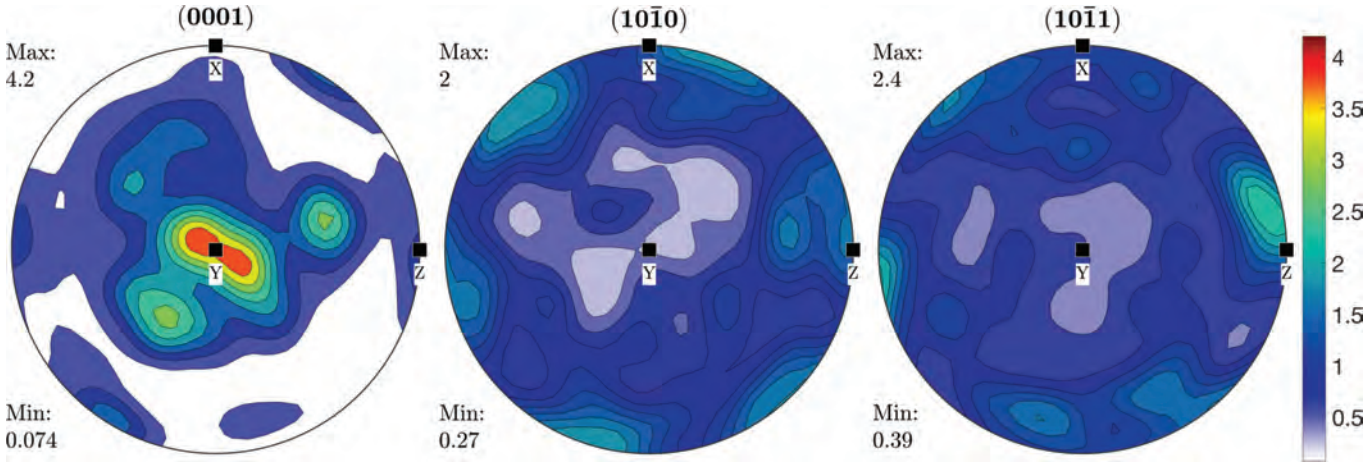

Figure 12

This is the peer-reviewed, final accepted version for American Mineralogist, published by the Mineralogical Society of America.
The published version is subject to change. Cite as Authors (Year) Title. American Mineralogist, in press.
DOI: https://doi.org/10.2138/am-2021-7902. http://www.minsocam.org/

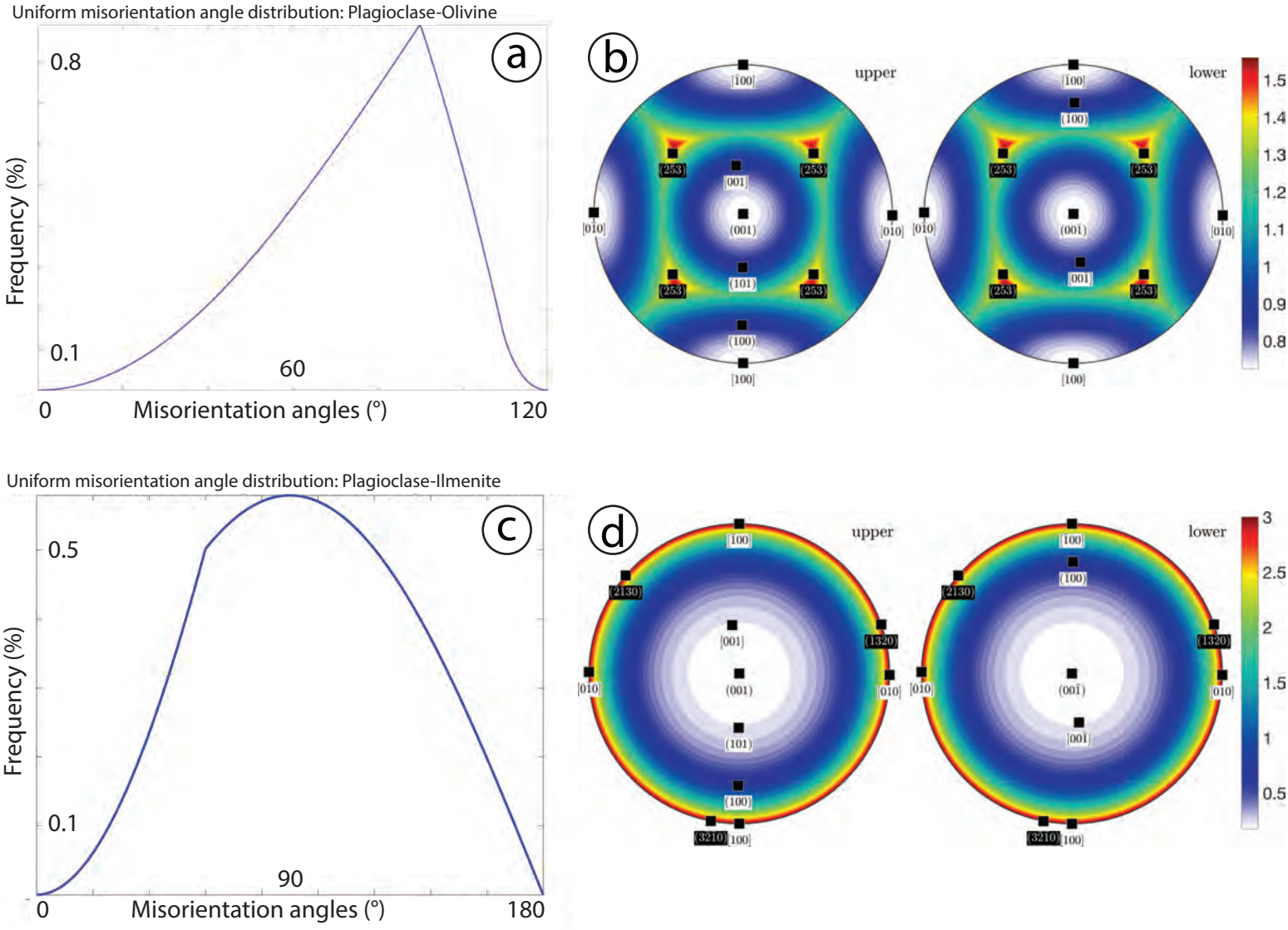

Figure 13

This is the peer-reviewed, final accepted version for American Mineralogist, published by the Mineralogical Society of America.
The published version is subject to change. Cite as Authors (Year) Title. American Mineralogist, in press.
DOI: https://doi.org/10.2138/am-2021-7902. http://www.minsocam.org/

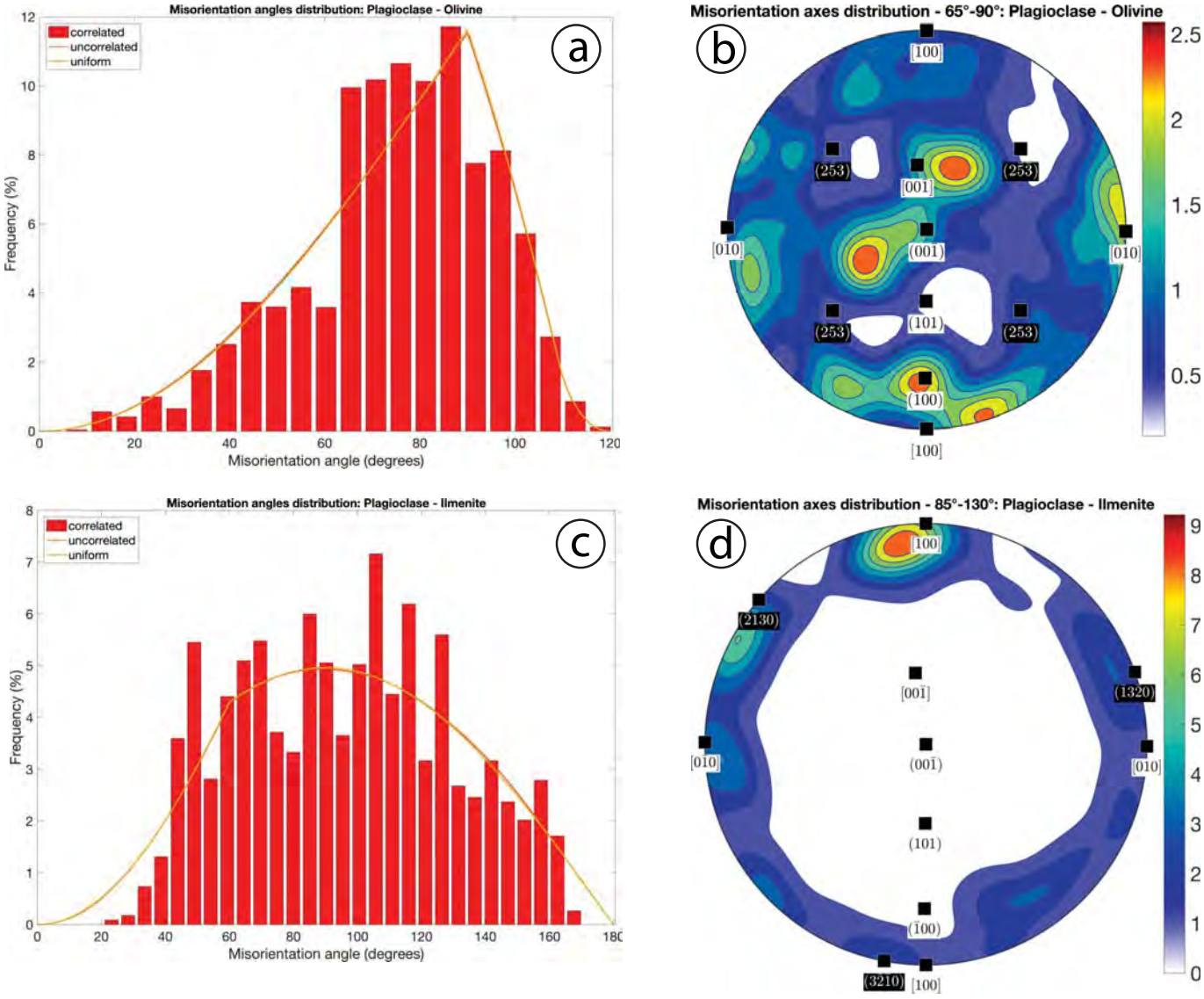

Figure 14

This is the peer-reviewed, final accepted version for American Mineralogist, published by the Mineralogical Society of America.
The published version is subject to change. Cite as Authors (Year) Title. American Mineralogist, in press.
DOI: https://doi.org/10.2138/am-2021-7902. http://www.minsocam.org/

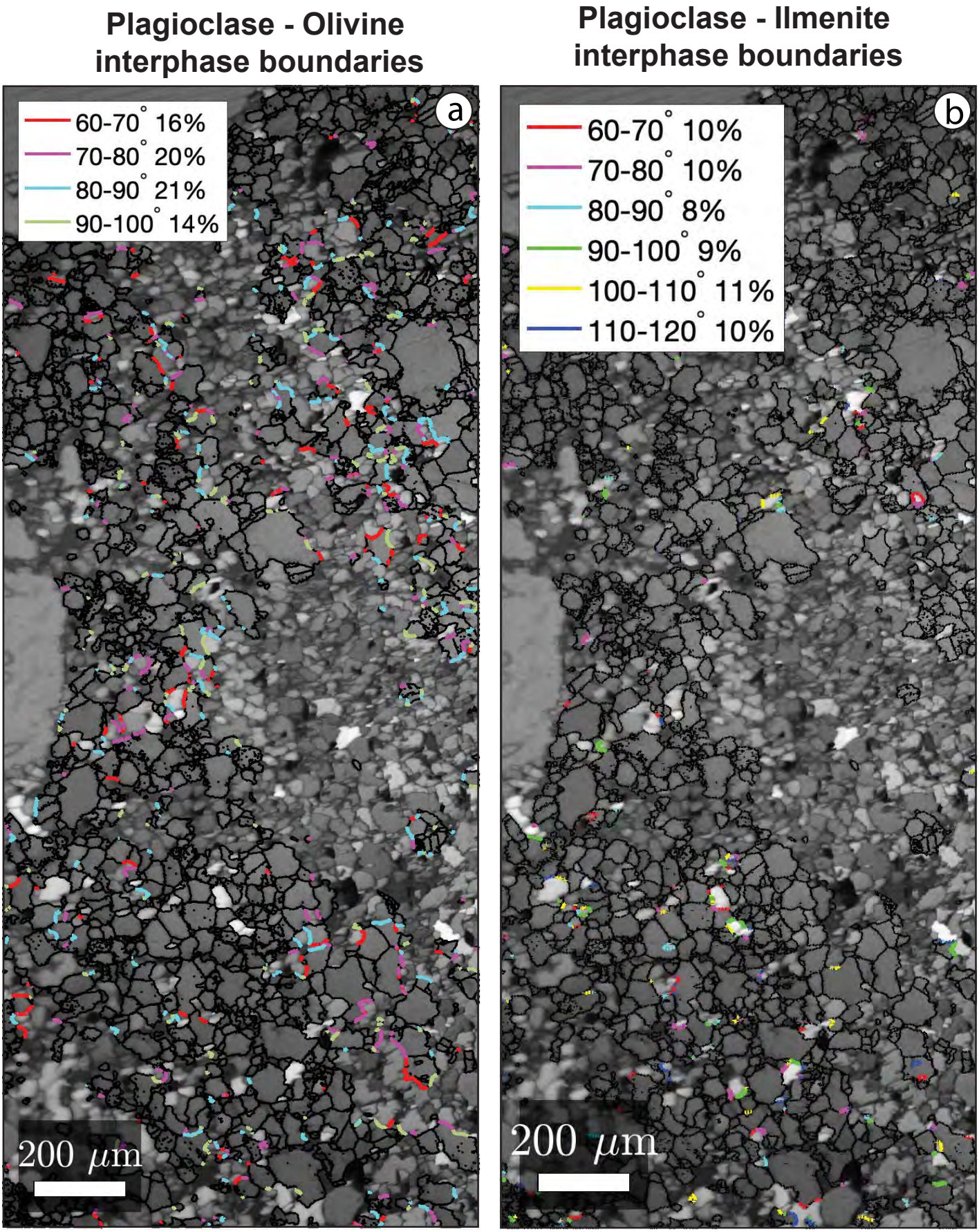

Figure 15